DESY 09-032 ISSN 0418-9833
November 2009

Jet Production in ep Collisions at High Q^2 and Determination of α_s

H1 Collaboration

Abstract

The production of jets is studied in deep-inelastic $e^{\pm}p$ scattering at large negative four momentum transfer squared $150 < Q^2 < 15000$ GeV^2 using HERA data taken in 1999-2007, corresponding to an integrated luminosity of $395\,\mathrm{pb}^{-1}$. Inclusive jet, 2-jet and 3-jet cross sections, normalised to the neutral current deep-inelastic scattering cross sections, are measured as functions of Q^2, jet transverse momentum and proton momentum fraction. The measurements are well described by perturbative QCD calculations at next-to-leading order corrected for hadronisation effects. The strong coupling as determined from these measurements is $\alpha_s(M_Z) = 0.1168 \ \pm 0.0007\,(\mathrm{exp.})\ ^{+0.0046}_{-0.0030}\,(\mathrm{th.})\ \pm 0.0016\,(\mathrm{PDF})$.

Accepted by *Eur. Phys. J.* **C**

F.D. Aaron[5,49], C. Alexa[5], K. Alimujiang[11], V. Andreev[25], B. Antunovic[11], A. Asmone[33], S. Backovic[30], A. Baghdasaryan[38], E. Barrelet[29], W. Bartel[11], K. Begzsuren[35], A. Belousov[25], J.C. Bizot[27], V. Boudry[28], I. Bozovic-Jelisavcic[2], J. Bracinik[3], G. Brandt[11], M. Brinkmann[12], V. Brisson[27], D. Bruncko[16], A. Bunyatyan[13,38], G. Buschhorn[26], L. Bystritskaya[24], A.J. Campbell[11], K.B. Cantun Avila[22], F. Cassol-Brunner[21], K. Cerny[32], V. Cerny[16,47], V. Chekelian[26], A. Cholewa[11], J.G. Contreras[22], J.A. Coughlan[6], G. Cozzika[10], J. Cvach[31], J.B. Dainton[18], K. Daum[37,43], M. Deák[11], Y. de Boer[11], B. Delcourt[27], M. Del Degan[40], J. Delvax[4], A. De Roeck[11,45], E.A. De Wolf[4], C. Diaconu[21], V. Dodonov[13], A. Dossanov[26], A. Dubak[30,46], G. Eckerlin[11], V. Efremenko[24], S. Egli[36], A. Eliseev[25], E. Elsen[11], A. Falkiewicz[7], P.J.W. Faulkner[3], L. Favart[4], A. Fedotov[24], R. Felst[11], J. Feltesse[10,48], J. Ferencei[16], D.-J. Fischer[11], M. Fleischer[11], A. Fomenko[25], E. Gabathuler[18], J. Gayler[11], S. Ghazaryan[38], A. Glazov[11], I. Glushkov[39], L. Goerlich[7], N. Gogitidze[25], M. Gouzevitch[11], C. Grab[40], T. Greenshaw[18], B.R. Grell[11], G. Grindhammer[26], S. Habib[12,50], D. Haidt[11], C. Helebrant[11], R.C.W. Henderson[17], E. Hennekemper[15], H. Henschel[39], M. Herbst[15], G. Herrera[23], M. Hildebrandt[36], K.H. Hiller[39], D. Hoffmann[21], R. Horisberger[36], T. Hreus[4,44], M. Jacquet[27], M.E. Janssen[11], X. Janssen[4], V. Jemanov[12], L. Jönsson[20], A.W. Jung[15], H. Jung[11], M. Kapichine[9], J. Katzy[11], I.R. Kenyon[3], C. Kiesling[26], M. Klein[18], C. Kleinwort[11], T. Kluge[18], A. Knutsson[11], R. Kogler[26], V. Korbel[11], P. Kostka[39], M. Kraemer[11], K. Krastev[11], J. Kretzschmar[18], A. Kropivnitskaya[24], K. Krüger[15], K. Kutak[11], M.P.J. Landon[19], W. Lange[39], G. Laštovička-Medin[30], P. Laycock[18], A. Lebedev[25], G. Leibenguth[40], V. Lendermann[15], S. Levonian[11], G. Li[27], K. Lipka[12], A. Liptaj[26], B. List[12], J. List[11], N. Loktionova[25], R. Lopez-Fernandez[23], V. Lubimov[24], L. Lytkin[13], A. Makankine[9], E. Malinovski[25], P. Marage[4], Ll. Marti[11], H.-U. Martyn[1], S.J. Maxfield[18], A. Mehta[18], A.B. Meyer[11], H. Meyer[11], H. Meyer[37], J. Meyer[11], V. Michels[11], S. Mikocki[7], I. Milcewicz-Mika[7], F. Moreau[28], A. Morozov[9], J.V. Morris[6], M.U. Mozer[4], M. Mudrinic[2], K. Müller[41], P. Murín[16,44], B. Naroska[12,†], Th. Naumann[39], P.R. Newman[3], C. Niebuhr[11], A. Nikiforov[11], G. Nowak[7], K. Nowak[41], M. Nozicka[11], B. Olivier[26], J.E. Olsson[11], S. Osman[20], D. Ozerov[24], V. Palichik[9], I. Panagoulias[l,11,42], M. Pandurovic[2], Th. Papadopoulou[l,11,42], C. Pascaud[27], G.D. Patel[18], O. Pejchal[32], E. Perez[10,45], A. Petrukhin[24], I. Picuric[30], S. Piec[39], D. Pitzl[11], R. Plačakytė[11], B. Pokorny[12], R. Polifka[32], B. Povh[13], T. Preda[5], V. Radescu[11], A.J. Rahmat[18], N. Raicevic[30], A. Raspiareza[26], T. Ravdandorj[35], P. Reimer[31], E. Rizvi[19], P. Robmann[41], B. Roland[4], R. Roosen[4], A. Rostovtsev[24], M. Rotaru[5], J.E. Ruiz Tabasco[22], Z. Rurikova[11], S. Rusakov[25], D. Šálek[32], D.P.C. Sankey[6], M. Sauter[40], E. Sauvan[21], S. Schmitt[11], C. Schmitz[41], L. Schoeffel[10], A. Schöning[14], H.-C. Schultz-Coulon[15], F. Sefkow[11], R.N. Shaw-West[3], I. Sheviakov[25], L.N. Shtarkov[25], S. Shushkevich[26], T. Sloan[17], I. Smiljanic[2], Y. Soloviev[25], P. Sopicki[7], D. South[8], V. Spaskov[9], A. Specka[28], Z. Staykova[11], M. Steder[11], B. Stella[33], G. Stoicea[5], U. Straumann[41], D. Sunar[4], T. Sykora[4], V. Tchoulakov[9], G. Thompson[19], P.D. Thompson[3], T. Toll[12], F. Tomasz[16], T.H. Tran[27], D. Traynor[19], T.N. Trinh[21], P. Truöl[41], I. Tsakov[34], B. Tseepeldorj[35,51], J. Turnau[7], K. Urban[15], A. Valkárová[32], C. Vallée[21], P. Van Mechelen[4], A. Vargas Trevino[11], Y. Vazdik[25], S. Vinokurova[11], V. Volchinski[38], M. von den Driesch[11], D. Wegener[8], Ch. Wissing[11], E. Wünsch[11], J. Žáček[32], J. Zálešák[31], Z. Zhang[27], A. Zhokin[24], T. Zimmermann[40], H. Zohrabyan[38], F. Zomer[27], and R. Zus[5]

[1] *I. Physikalisches Institut der RWTH, Aachen, Germany*[a]

[2] *Vinca Institute of Nuclear Sciences, Belgrade, Serbia*

[3] *School of Physics and Astronomy, University of Birmingham, Birmingham, UK*[b]
[4] *Inter-University Institute for High Energies ULB-VUB, Brussels; Universiteit Antwerpen, Antwerpen; Belgium*[c]
[5] *National Institute for Physics and Nuclear Engineering (NIPNE) , Bucharest, Romania*
[6] *Rutherford Appleton Laboratory, Chilton, Didcot, UK*[b]
[7] *Institute for Nuclear Physics, Cracow, Poland*[d]
[8] *Institut für Physik, TU Dortmund, Dortmund, Germany*[a]
[9] *Joint Institute for Nuclear Research, Dubna, Russia*
[10] *CEA, DSM/Irfu, CE-Saclay, Gif-sur-Yvette, France*
[11] *DESY, Hamburg, Germany*
[12] *Institut für Experimentalphysik, Universität Hamburg, Hamburg, Germany*[a]
[13] *Max-Planck-Institut für Kernphysik, Heidelberg, Germany*
[14] *Physikalisches Institut, Universität Heidelberg, Heidelberg, Germany*[a]
[15] *Kirchhoff-Institut für Physik, Universität Heidelberg, Heidelberg, Germany*[a]
[16] *Institute of Experimental Physics, Slovak Academy of Sciences, Košice, Slovak Republic*[f]
[17] *Department of Physics, University of Lancaster, Lancaster, UK*[b]
[18] *Department of Physics, University of Liverpool, Liverpool, UK*[b]
[19] *Queen Mary and Westfield College, London, UK*[b]
[20] *Physics Department, University of Lund, Lund, Sweden*[g]
[21] *CPPM, CNRS/IN2P3 - Univ. Mediterranee, Marseille, France*
[22] *Departamento de Fisica Aplicada, CINVESTAV, Mérida, Yucatán, México*[j]
[23] *Departamento de Fisica, CINVESTAV, México*[j]
[24] *Institute for Theoretical and Experimental Physics, Moscow, Russia*[k]
[25] *Lebedev Physical Institute, Moscow, Russia*[e]
[26] *Max-Planck-Institut für Physik, München, Germany*
[27] *LAL, Univ Paris-Sud, CNRS/IN2P3, Orsay, France*
[28] *LLR, Ecole Polytechnique, IN2P3-CNRS, Palaiseau, France*
[29] *LPNHE, Universités Paris VI and VII, IN2P3-CNRS, Paris, France*
[30] *Faculty of Science, University of Montenegro, Podgorica, Montenegro*[e]
[31] *Institute of Physics, Academy of Sciences of the Czech Republic, Praha, Czech Republic*[h]
[32] *Faculty of Mathematics and Physics, Charles University, Praha, Czech Republic*[h]
[33] *Dipartimento di Fisica Università di Roma Tre and INFN Roma 3, Roma, Italy*
[34] *Institute for Nuclear Research and Nuclear Energy, Sofia, Bulgaria*[e]
[35] *Institute of Physics and Technology of the Mongolian Academy of Sciences , Ulaanbaatar, Mongolia*
[36] *Paul Scherrer Institut, Villigen, Switzerland*
[37] *Fachbereich C, Universität Wuppertal, Wuppertal, Germany*
[38] *Yerevan Physics Institute, Yerevan, Armenia*
[39] *DESY, Zeuthen, Germany*
[40] *Institut für Teilchenphysik, ETH, Zürich, Switzerland*[i]
[41] *Physik-Institut der Universität Zürich, Zürich, Switzerland*[i]

[42] *Also at Physics Department, National Technical University, Zografou Campus, GR-15773 Athens, Greece*
[43] *Also at Rechenzentrum, Universität Wuppertal, Wuppertal, Germany*
[44] *Also at University of P.J. Šafárik, Košice, Slovak Republic*

[45] *Also at CERN, Geneva, Switzerland*
[46] *Also at Max-Planck-Institut für Physik, München, Germany*
[47] *Also at Comenius University, Bratislava, Slovak Republic*
[48] *Also at DESY and University Hamburg, Helmholtz Humboldt Research Award*
[49] *Also at Faculty of Physics, University of Bucharest, Bucharest, Romania*
[50] *Supported by a scholarship of the World Laboratory Björn Wiik Research Project*
[51] *Also at Ulaanbaatar University, Ulaanbaatar, Mongolia*
† *Deceased*

[a] *Supported by the Bundesministerium für Bildung und Forschung, FRG, under contract numbers 05 H1 1GUA /1, 05 H1 1PAA /1, 05 H1 1PAB /9, 05 H1 1PEA /6, 05 H1 1VHA /7 and 05 H1 1VHB /5*
[b] *Supported by the UK Science and Technology Facilities Council, and formerly by the UK Particle Physics and Astronomy Research Council*
[c] *Supported by FNRS-FWO-Vlaanderen, IISN-IIKW and IWT and by Interuniversity Attraction Poles Programme, Belgian Science Policy*
[d] *Partially Supported by Polish Ministry of Science and Higher Education, grant PBS/DESY/70/2006*
[e] *Supported by the Deutsche Forschungsgemeinschaft*
[f] *Supported by VEGA SR grant no. 2/7062/ 27*
[g] *Supported by the Swedish Natural Science Research Council*
[h] *Supported by the Ministry of Education of the Czech Republic under the projects LC527, INGO-1P05LA259 and MSM0021620859*
[i] *Supported by the Swiss National Science Foundation*
[j] *Supported by CONACYT, México, grant 48778-F*
[k] *Russian Foundation for Basic Research (RFBR), grant no 1329.2008.2*
[l] *This project is co-funded by the European Social Fund (75%) and National Resources (25%) - (EPEAEK II) - PYTHAGORAS II*

1 Introduction

Jet production in neutral current (NC) deep-inelastic scattering (DIS) at HERA provides an important testing ground for Quantum Chromodynamics (QCD). While inclusive DIS gives only indirect information on the strong coupling via scaling violations of the proton structure functions, the production of jets allows a direct measurement of α_s. The Born level contribution to DIS (figure 1a) generates no transverse momentum in the Breit frame, where the virtual boson and the proton collide head on [1]. Significant transverse momentum P_T in the Breit frame is produced at leading order (LO) in the strong coupling α_s by the QCD-Compton (figure 1b) and boson-gluon fusion (figure 1c) processes.

In leading order the proton's momentum fraction carried by the emerging parton is given by $\xi = x_{\mathrm{Bj}}(1 + M_{12}^2/Q^2)$. The variable x_{Bj} denotes the Bjorken scaling variable, M_{12} the invariant mass of two jets of highest P_T and Q^2 the negative four momentum transfer squared. In the kinematical regions of low Q^2, low P_T and low ξ, boson-gluon fusion dominates the jet production and provides direct sensitivity to the gluon component of proton density functions (PDFs) [2].

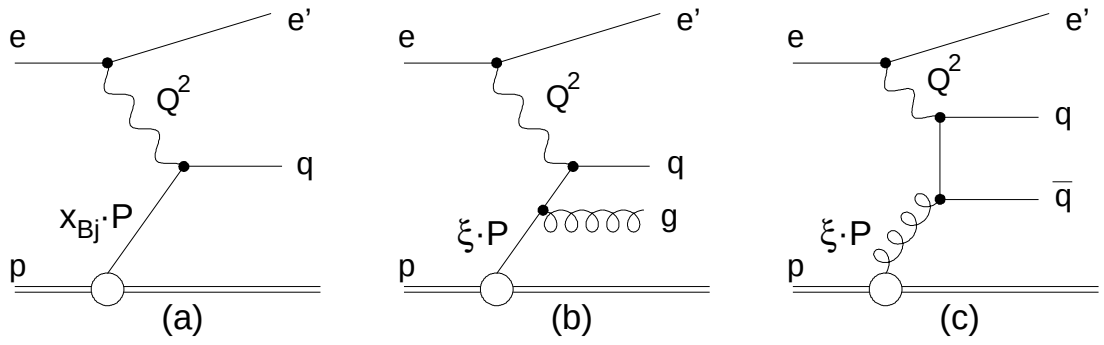

Figure 1: Deep-inelastic lepton-proton scattering at different orders in α_s: (a) Born contribution $\mathcal{O}(1)$, (b) example of the QCD Compton scattering $\mathcal{O}(\alpha_s)$ and (c) boson-gluon fusion $\mathcal{O}(\alpha_s)$.

Analyses of inclusive jet production in DIS at high Q^2 were previously performed by the H1 [3] and ZEUS [4] collaborations at HERA. These analyses are based on data taken during 1999 and 2000 (HERA-I) and use jet observables to test the running of the strong coupling and extract its value at the Z^0 boson mass. In this paper an integrated luminosity six times larger than available in the previous H1 analysis [3] is used. The ratios of jet cross sections to the corresponding NC DIS cross sections, henceforth referred to as normalised jet cross sections, are measured. These ratios benefit from a partial cancellation of experimental and theoretical uncertainties. The measurements are compared with perturbative QCD (pQCD) predictions at next-to-leading order (NLO) corrected for hadronisation effects, and α_s is extracted from a fit of the predictions to the data. The measurements presented in this paper supersede the previously published normalised jet cross sections in [3].

2 Experimental Method

The data sample was collected with the H1 detector at HERA in the years 1999 to 2007 when HERA collided electrons or positrons[1] of energy $E_e = 27.6$ GeV with protons of energy $E_p = 920$ GeV, providing a centre-of-mass energy $\sqrt{s} = 319$ GeV. The data sample used in this analysis corresponds to an integrated luminosity of $395\,\text{pb}^{-1}$, comprising $153\,\text{pb}^{-1}$ recorded in e^-p collisions and $242\,\text{pb}^{-1}$ in e^+p collisions.

2.1 H1 detector

A detailed description of the H1 detector can be found in [5, 6]. H1 uses a right-handed coordinate system with the origin at the nominal interaction point and the z-axis along the beam direction. The positive z direction, also called the forward direction, is given by the outgoing proton beam. Polar angles θ and azimuthal angles ϕ are defined with respect to this axis. The pseudorapidity is related to the polar angle θ by $\eta = -\ln\tan(\theta/2)$. The detector components important for this analysis are described below.

The electromagnetic and hadronic energies are measured using the Liquid Argon (LAr) calorimeter in the polar angular range $4^\circ < \theta < 154^\circ$ and with full azimuthal coverage [7]. The LAr calorimeter consists of an electromagnetic section (20 to 30 radiation lengths) with lead absorbers and a hadronic section with steel absorbers. The total depth of the LAr calorimeter varies between 4.5 and 8 hadronic interaction lengths. The energy resolution is $\sigma_E/E = 12\%/\sqrt{E\ /\,\text{GeV}} \oplus 1\%$ for electrons and $\sigma_E/E = 50\%/\sqrt{E\ /\,\text{GeV}} \oplus 2\%$ for hadrons, as obtained from test beam measurements [8]. In the backward region ($153^\circ \leq \theta \leq 177^\circ$) energy is measured by a lead/scintillating fibre Spaghetti-type Calorimeter (SpaCal) composed of an electromagnetic and a hadronic section [6]. The central tracking system ($20^\circ \leq \theta \leq 160^\circ$) is located inside the LAr calorimeter and consists of drift and proportional chambers, complemented by a silicon vertex detector covering the range $30^\circ \leq \theta \leq 150^\circ$ [9]. The chambers and calorimeters are surrounded by a superconducting solenoid providing a uniform field of 1.16 T inside the tracking volume. The luminosity is determined by measuring the event rate of the Bethe-Heitler process ($ep \to ep\gamma$), where the photon is detected in a calorimeter close to the beam pipe at $z = -103$ m.

2.2 Event and jet selection

The NC DIS events are triggered and selected by requiring a compact energy deposit in the electromagnetic part of the LAr calorimeter. The scattered electron is identified as the isolated cluster of highest transverse momentum [10]. Its reconstructed energy is requested to exceed 11 GeV. Only the regions of the calorimeter where the trigger efficiency is greater than 98% are used for the detection of the scattered electron. These requirements ensure that the overall trigger efficiency reaches 99.5%. In the central region, $30^\circ \leq \theta \leq 155^\circ$, the cluster has to be associated with a track measured in the inner tracking chambers and matched to the primary

[1] Unless otherwise stated, the term "electron" is used in the following to refer to both electron and positron.

event vertex. The z-coordinate of the primary event vertex is required to be within ± 35 cm of the nominal position of the interaction point.

The remaining clusters in the calorimeters and charged tracks are attributed to the hadronic final state, which is reconstructed using an energy flow algorithm that avoids double counting of energy [11, 12]. Electromagnetic and hadronic energy calibration and the alignment of the H1 detector are performed following the same procedure as in [10]. The total longitudinal energy balance, calculated as the difference of the total energy E and the longitudinal component of the total momentum P_z, calculated from all detected particles including the scattered electron, must satisfy $35 < E - P_z < 65$ GeV. This requirement reduces contributions of DIS events with hard initial state photon radiation. For the latter events, the undetected photons propagating in the negative z direction lead to values of this observable significantly lower than the expected value of $2E_e = 55.2\,\text{GeV}$. The $E - P_z$ requirement together with the scattered electron selection also reduces contributions from photoproduction, estimated using Monte Carlo simulations. Cosmic muon and beam induced background is reduced to a negligible level after combining these cuts with the primary event vertex selection. Elastic QED Compton and lepton pair production processes are suppressed by rejecting events containing additional isolated electromagnetic deposits and low hadronic calorimeter activity.

The kinematical range of this analysis is defined by

$$150 < Q^2 < 15000\,\text{GeV}^2 \quad \text{and} \quad 0.2 < y < 0.7\,,$$

where $y = Q^2/(s\,x_{\text{Bj}})$ quantifies the inelasticity of the interaction. These two variables are reconstructed from the four momenta of the scattered electron and the hadronic final state particles using the electron-sigma method [13]. The selection of events passing all the above cuts is the NC DIS sample, which forms the basis of the subsequent analysis.

The jet finding is performed in the Breit frame, where the boost from the laboratory system is determined by Q^2, y and by the azimuthal angle ϕ_e of the scattered electron. Particles of the hadronic final state are clustered into jets using the inclusive k_T algorithm [14] with the massless P_T recombination scheme and with the distance parameter $R_0 = 1$ in the $\eta - \phi$ plane. The cut $-0.8 < \eta^{\text{jet}}_{\text{Lab}} < 2.0$, where $\eta^{\text{jet}}_{\text{Lab}}$ is the jet pseudorapidity in the laboratory frame, ensures that jets are contained within the acceptance of the LAr calorimeter and are well calibrated.

Jets are ordered by decreasing transverse momentum P_T in the Breit frame, which is identical to the transverse energy E_T for massless jets. The jet with highest P_T is referred to as the "leading jet". Every jet with the transverse momentum P_T in the Breit frame satisfying $7 < P_T < 50\,\text{GeV}$ contributes to the inclusive jet cross section. The upper cutoff is necessary for the integration of the NLO calculation. The steeply falling transverse momentum spectrum leaves almost no jets above 50 GeV. Events with at least two (three) jets with transverse momentum $5 < P_T < 50\,\text{GeV}$ are considered as 2-jet (3-jet) events. In order to avoid regions of phase-space where fixed order perturbation theory is not reliable [15], 2-jet events are accepted only if the invariant mass M_{12} of the two leading jets exceeds $16\,\text{GeV}$. The same requirement, $M_{12} > 16\,\text{GeV}$, is applied to the 3-jet events so that the 3-jet sample is a subset of the 2-jet sample.

After this selection, the inclusive jet sample contains a total of 143811 jets in 104014 events. The 2-jet sample contains 47278 events and the 3-jet sample 7054 events.

2.3 Definition of the observables

The measurements presented in this paper refer to the phase-space given in table 1. Normalised inclusive jet cross sections are measured as functions of Q^2 and double differentially as function of Q^2 and the transverse jet momentum P_T in the Breit frame. Normalised 2-jet and 3-jet cross sections are presented as a function of Q^2. In addition the 2-jet cross sections are measured double differentially as function of Q^2 and the average transverse momentum of the two leading jets $\langle P_T \rangle = \frac{1}{2} \cdot (P_T^{\mathrm{jet}\,1} + P_T^{\mathrm{jet}\,2})$ or as function of Q^2 and of the proton momentum fraction ξ. The 3-jet cross section normalised to the 2-jet cross section as function of Q^2 is also presented.

The normalised jet cross sections are defined as the ratio of the differential inclusive jet, 2-jet and 3-jet cross sections to the differential NC DIS cross section in a given Q^2 bin, multiplied by the respective bin width W in case of a double differential measurement as indicated by the following equations:

$$\frac{\sigma_{\mathrm{jet}}}{\sigma_{\mathrm{NC}}}\left(Q^2,\, P_T\right) = \frac{\mathrm{d}^2\sigma_{\mathrm{jet}}/\mathrm{d}Q^2\,\mathrm{d}P_T}{\mathrm{d}\sigma_{\mathrm{NC}}/\mathrm{d}Q^2} \cdot W(P_T) \tag{1}$$

$$\frac{\sigma_{\text{2-jet}}}{\sigma_{\mathrm{NC}}}\left(Q^2,\, \langle P_T \rangle\right) = \frac{\mathrm{d}^2\sigma_{\text{2-jet}}/\mathrm{d}Q^2\,\mathrm{d}\langle P_T \rangle}{\mathrm{d}\sigma_{\mathrm{NC}}/\mathrm{d}Q^2} \cdot W(\langle P_T \rangle) \tag{2}$$

$$\frac{\sigma_{\text{2-jet}}}{\sigma_{\mathrm{NC}}}\left(Q^2,\, \xi\right) = \frac{\mathrm{d}^2\sigma_{\text{2-jet}}/\mathrm{d}Q^2\,\mathrm{d}\xi}{\mathrm{d}\sigma_{\mathrm{NC}}/\mathrm{d}Q^2} \cdot W(\xi) \tag{3}$$

The normalised inclusive jet cross section can be viewed as the average jet multiplicity in a given Q^2 region and the normalised multi-jet cross sections as multi-jet event rates.

2.4 Determination of normalised cross sections

In each analysis bin the normalised jet cross section is determined as

$$\frac{\sigma_{\mathrm{J}}}{\sigma_{\mathrm{NC}}} = \frac{N_{\mathrm{J}}}{N_{\mathrm{NC}}} \cdot C\,. \tag{4}$$

Here N_{J} denotes the number of inclusive jets or the number of 2-jet or 3-jet events, respectively, while N_{NC} represents the number of NC DIS events in that bin. The bin dependent correction factor C takes into account the limited detector acceptance and resolution. The correction factors are determined from Monte Carlo simulations as the ratio of the normalised jet cross sections obtained from particles at the hadron level to the normalised jet cross sections calculated using reconstructed particles.

The following LO Monte Carlo event generators are used for the correction procedure: DJANGOH [16], which uses the Color Dipole Model with QCD matrix element corrections as implemented in ARIADNE [17], and RAPGAP [18], based on QCD matrix elements matched with parton showers in leading log approximation. In both Monte Carlo generators the hadronisation is modelled with Lund string fragmentation [19]. All generated events are passed through a GEANT3 [20] based simulation of the H1 apparatus and are reconstructed using the same program chain as for the data. Both RAPGAP and DJANGOH provide a good overall description

of the inclusive DIS sample. To further improve the agreement between Monte Carlo and data for the jet samples, the Monte Carlo events are weighted as a function of Q^2 and y and as function of P_T and η of the leading jet in the Breit frame. In addition, they are weighted as a function of P_T of the second and third jets when present [21]. After weighting, the simulations provide a good description of the shapes of all data distributions, some of which are shown in figure 2.

The binnings in Q^2, P_T and ξ used to measure the jet observables are given in table 2. The associated bin purities, defined as the fraction of the events reconstructed in a particular bin that originate from that bin on the generator level, are typically 70% and always greater than 60%. The correction factors deviate typically by less than 20% from unity, but reach 40% difference from unity in the bin $5 < \langle P_T \rangle < 7$ GeV for the 2-jet cross section. Arithmetic means of the correction factors determined from the reweighted RAPGAP and DJANGOH event samples are used and half of the difference is assigned as a model uncertainty.

The above correction factors include QED radiation and electroweak effects. The effects of QED radiation, which are typically 5%, are corrected for by means of the HERACLES [22] program. The LEPTO event generator [23] is used to correct the e^+p and e^-p data for their different electroweak effects which largely cancel in normalised jet cross sections leaving them below 3%. The resulting pure photon exchange cross sections obtained from e^+p and e^-p data samples are then averaged.

2.5 Experimental uncertainties

The systematic uncertainties of the jet observables are determined by propagating the corresponding estimated measurement errors through the full analysis:

- The relative uncertainty of the electron energy calibration is typically between 0.7% and 1% for most of the events and increases up to 2% for electrons in the forward direction. The absolute uncertainty of the electron polar angle is 3 mrad. Uncertainties in the electron reconstruction affect the event kinematics and thus the boost to the Breit frame. This in turn leads to a relative error of 0.5% to 1.5% on the normalised cross sections for each of the two sources, electron polar angle and energy.

- The relative uncertainty on the energy of the total reconstructed hadronic final state as well as of jets is estimated to be 1.5% [21]. It is dominated by the uncertainty of the hadronic energy scale of the calorimeter. This error is estimated using a procedure similar to that used in [10] based on the transverse momentum conservation in the laboratory frame between the hadronic final state $P_{T,h}$ and the electron $P_{T,e}$. This systematic uncertainty is reduced with respect to the previous measurement [3] due to the restricted pseudorapidity range in which jets are reconstructed and due to the improved statistics in the calibration procedure. The hadronic energy scale uncertainty affects mainly the jet cross section through the calibration of P_T and, to a lesser extent, the NC DIS cross section through the reconstruction of y. The resulting errors range between 1% and 5% and increase up to 7% when P_T exceeds 30 GeV. The relative uncertainty due to the hadronic energy scale is reduced on average by about 20% for the normalised jet cross sections compared to the jet cross sections.

- The model dependence of the detector correction factors is estimated as described in section 2.4. It reflects the sensitivity of the detector simulation to the details of the model, especially the parton showering, and their impact on the migration between adjacent bins in P_T. The model dependence ranges typically from 1% to 2% for P_T below 30 GeV and to 4% above, independently of Q^2.

- The uncertainties of the luminosity measurements, the trigger efficiency and the electron identification efficiency cancel in the normalised cross section. In addition, the model dependence of the QED radiative corrections, which is estimated to be 1% [10], is expected to cancel in the normalised cross sections.

The statistical errors for the normalised inclusive jet cross section take into account the statistical correlations which arise because there can be more than one jet per event [21]. The statistical errors are considerably smaller compared to the previous HERA-I publication [3]. They are typically between 1% and 2% for the normalised inclusive and 2-jet cross sections and do not exceed 10% in the regions of high transverse momentum P_T or high boson virtuality Q^2.

The dominant experimental errors on the jet cross sections arise from the uncertainty on the hadronic energy scale. The second most important source of systematic errors is the model dependence of the data correction, which becomes comparable to or exceeds the former in regions of highest jet P_T. The overall experimental error, calculated as the quadratic sum of all the contributions inventoried above, ranges typically between 3% and 6%, but increases up to 15% in the regions of highest P_T or Q^2, dominated there by statistical uncertainties. The experimental errors for normalised cross sections are reduced by 30% up to 50% compared to those for unnormalised cross sections.

3 NLO QCD prediction of jet cross sections

Reliable quantitative predictions of jet cross sections in DIS require the perturbative calculations to be performed at least to next-to-leading order in the strong coupling. By using the inclusive k_T jet algorithm with radius parameter $R = 1$, the observables used in the present analysis are infrared and collinear safe and the non-perturbative effects are expected to be small [2]. In addition, applying this algorithm in the Breit frame has the advantage that initial state singularities can be absorbed in the definition of the proton parton densities [24].

Jet cross sections are predicted at the parton level using the same jet definition as in the data analysis. The QCD predictions for the jet cross sections are calculated using the NLOJET++ program at NLO in the strong coupling [25]. The NC DIS cross section is calculated at $\mathcal{O}(\alpha_s)$ with the DISENT package [26]. The FastNLO program [27] provides an efficient method to calculate these cross sections based on matrix elements from NLOJET++ and DISENT, convoluted with the PDFs of the proton and as a function of α_s. The program includes a coherent treatment of the renormalisation and factorisation scale dependences of all ingredients to the cross section calculation, namely the matrix elements, the PDFs and α_s.

When comparing data and theory predictions the strong coupling at the Z^0 boson mass is taken to be $\alpha_s(M_Z) = 0.1168$ and is evolved as a function of the renormalisation scale

with two loop precision. The calculations are performed in the $\overline{MS}$ scheme for five massless quark flavours. The PDFs of the proton are taken from the CTEQ6.5M set [28]. The factorisation scale μ_f is taken to be Q and the renormalisation scale μ_r to be $\sqrt{(Q^2 + P_{T,\,\mathrm{obs}}^2)/2}$ for the NLO predictions, with $P_{T,\mathrm{obs}}$ denoting P_T for the inclusive jet, $\langle P_T \rangle$ for 2-jet and $\frac{1}{3} \cdot (P_T^{\mathrm{jet}1} + P_T^{\mathrm{jet}2} + P_T^{\mathrm{jet}3})$ for the 3-jet cross sections. This choice of the renormalisation scale is motivated by the presence of two hard scales, P_T and Q in the jet production in DIS. For the calculation of inclusive DIS cross sections, the renormalisation scale $\mu_r = Q$ is used. No QED radiation or Z^0 exchange is included in the calculations, but the running of the electromagnetic coupling with Q^2 is taken into account.

Hadronisation corrections are calculated for each bin using Monte Carlo event generators. These corrections are determined as the ratio of the cross section at the hadron level to the cross section at the parton level after parton showers. They typically differ by less than 10% from unity and are obtained using the event generators DJANGOH and RAPGAP which agree to within 2% to 4%. The arithmetic means of the two Monte Carlo hadronisation correction factors are used, while the full difference is considered as systematic error.

DJANGOH and RAPGAP both use the Lund string model of hadronisation. The analytic calculations carried out in [29] provide an alternative method to estimate the effects of hadronisation and to cross-check the hadronisation correction procedure described above. They are based on soft gluon power corrections and result in a shift of the perturbatively calculated spectrum of the inclusive jets:

$$\frac{\mathrm{d}\sigma_{\mathrm{jet}}}{\mathrm{d}Q^2 \mathrm{d}P_T}\,(P_T) \approx \frac{\mathrm{d}\sigma_{\mathrm{jet}}^{\mathrm{NLO}}}{\mathrm{d}Q^2 \mathrm{d}P_T}\,(P_T - \delta\,\langle P_T \rangle_{\mathrm{NP}}) \tag{5}$$

The size of the non-perturbative shift $\delta\,\langle P_T \rangle_{\mathrm{NP}}$ can be calculated up to one single non-perturbative parameter $\alpha_0(\mu_I) = \mu_I^{-1} \int_0^{\mu_I} \alpha_{\mathrm{eff}}(k) dk$, which is the first moment of the effective non-perturbative coupling $\alpha_{\mathrm{eff}}(\mu)$ matched to the strong coupling $\alpha_s(\mu)$ at the scale μ_I. The value of $\alpha_0(\mu_I)$, expected to be universal [30], was measured to be $\alpha_0(\mu_I = 2\,\mathrm{GeV}) \approx 0.5$ using event shapes observables in DIS by the H1 Collaboration [31]. The hadronisation correction factors so calculated for the inclusive jet cross section differ in most of the bins by less than 2% from the average correction factor obtained from DJANGOH and RAPGAP and the maximum difference in all bins does not exceed 5% which is within the estimated uncertainty of the hadronisation correction.

The dominant theoretical error is due to the uncertainty related to the neglected higher orders in the perturbative calculation. The accuracy of the NLO calculation is conventionally estimated by separately varying the chosen scales for μ_f and μ_r by factors in the arbitrary range 0.5 to 2. At high transverse momentum, above 30 GeV, the pQCD calculations do not depend monotonically on μ_r in some Q^2 bins. This happens in the two highest Q^2 bins for the inclusive jet cross section and in six Q^2 bins for the 2-jet cross section, where the largest deviation from the central value is found for factors well inside the range 0.5 to 2. In such cases the difference between maximum and minimum cross sections found in the variation interval is taken, in order not to underestimate the scale dependence. Renormalisation and factorisation scale uncertainties are added in quadrature, the former outweighing the latter by a factor of two on average. The uncertainties originating from the PDFs are estimated using the CTEQ6.5M set of parton densities.

Normalised jet cross sections are calculated by dividing the predicted jet cross sections by the NC DIS cross sections. The renormalisation scale uncertainties are assumed to be uncorrelated between NC DIS and jet cross sections, as well as between 3-jet and 2-jet cross sections for their ratio, whereas the factorisation scale and the parameterisation uncertainty of the PDFs are assumed to be fully correlated.

4 Results

In the following, the normalised differential cross sections are presented for inclusive jet, 2-jet and 3-jet production at the hadron level. Tables 3 to 6 and figures 3 to 6 present the measured observables together with their experimental uncertainties and hadronisation correction factors applied to the NLO predictions. These measurements are subsequently used to extract the strong coupling α_s as shown in the table 9 and figures 7 to 12.

4.1 Cross section measurements compared to NLO predictions

The normalised inclusive jet cross sections as a function of Q^2 are shown in figure 3a and table 3 together with the NLO predictions and previous measurements by H1 based on HERA-I data [3]. For comparison, the HERA-I data points were corrected for the phase space difference due to the slightly smaller jet pseudorapidity range of the present analysis. The double differential results as a function of P_T in six ranges of Q^2 are given in figure 4 and table 4. Normalised 2-jet (3-jet) cross sections as a function of Q^2 and their comparison to NLO are also shown in figure 3b (3c) and table 3, while the ratio 3-jet to 2-jet is shown in figure 3d. Figures 5, 6 and tables 5, 6 present the normalised 2-jet cross section as a function of $\langle P_T \rangle$ and ξ in six ranges of Q^2.

The new measurement of the normalised inclusive jet cross section is compatible with the previous H1 data. The precision is improved by typically a factor of two, as can be seen for example in figure 3a. The QCD NLO predictions for all normalised jet cross sections provide a good description of the data over the whole phase space. In almost all bins the theory error, dominated by the μ_r scale uncertainty, is significantly larger than the total experimental uncertainty, which is dominated by the hadronic energy scale uncertainty.

The normalised inclusive jet cross section, which may be interpreted as the average jet multiplicity produced in NC DIS, increases with Q^2 as the available phase space opens (figure 3a) as do the 2-jet and 3-jet rates (figure 3b and 3c). As Q^2 increases, the P_T jet spectra become harder as can be seen in figure 4 and 5. The 3-jet rate is observed to be nearly seven times smaller than the 2-jet rate as shown in figure 3d. The 2-jet rates measured as a function of Q^2 and the momentum fraction ξ are well described by the NLO calculations (figure 6). Kinematic constraints from the considered y range and the restricted invariant mass of the jets lead to a reduction of the 2-jet rate at low ξ and a rise at large ξ with increasing Q^2.

4.2 Extraction of the strong coupling

The QCD predictions for jet production depend on α_s and on the parton density functions of the proton. The strong coupling α_s is determined from the measured normalised jet cross sections using the parton density functions from global analyses, which include inclusive deep-inelastic scattering and other data. The determination is performed from individual observables and also from their combination.

QCD predictions of the jet cross sections are calculated as a function of $\alpha_s(\mu_r)$ with the FastNLO package using the CTEQ6.5M proton PDFs and applying the hadronisation corrections as described in section 3. Measurements and theory predictions are used to calculate a $\chi^2(\alpha_s)$ with the Hessian method [33], where parameters representing systematic shifts of detector related observables are left free in the fit. The shifts in the electron energy scale, electron polar angle and the hadronic final state energy scale found by the fit are consistent with the *a priori* estimated uncertainties. This method takes into account correlations of experimental uncertainties and has also been used in global data analyses [33, 34] and in previous H1 publications [3, 35]. The experimental uncertainty of α_s is defined by the change in α_s which gives an increase in χ^2 of one unit with respect to the minimal value.

The correlations of the experimental uncertainties between data points were estimated using Monte Carlo simulations:

- The statistical correlations between different observables using the same events are taken into account via the correlation matrix given in tables 7 and 8.
- It is estimated that the uncertainty of the LAr hadronic energy scale is equally shared between correlated and uncorrelated contributions [3, 21], while that from the electron energy scale is estimated to be $3/4$ uncorrelated [10].
- The measurement of the electron polar angle is assumed to be fully correlated [10].
- The model dependence of the experimental correction factors is considered as fully uncorrelated after the averaging procedure described in section 2.5.

The sharing of correlated and uncorrelated contributions between the different sources of uncertainty has the following impact on the α_s determination: when going from uncorrelated to fully correlated error for each source, the fitted value of α_s typically varies by half the total experimental error and the estimated uncertainty by less than 0.1% of α_s.

The theory error is estimated by the so called *offset* method as the difference between the value of α_s from the nominal fit to the value when the fit is repeated with independent variations of different sources of theoretical uncertainties as described in section 3. The resulting uncertainties due to the different sources are summed in quadrature. The up (or down) variations are applied simultaneously to all bins in the fit. The impact of hadronisation corrections on α_s is between 0.4% and 1.0%, while that of the factorisation scale amounts to 0.5%. The sensitivity of α_s to the renormalisation scale variation of the inclusive NC DIS cross section alone is typically 0.5%. The largest uncertainty, of typically 3% to 4%, corresponds to the accuracy of the NLO approximation to the jet cross sections estimated by varying the renormalisation scale as

described in section 3. An alternative method to estimate the impact of missing orders, called the band method, developed by Jones et al. [36] was tested and, for the present measurement, it leads to a smaller uncertainty on α_s of typically 2%.

The uncertainty due to PDFs is estimated by propagating the CTEQ6.5M errors. The typical size of the resulting error is 1.5% for α_s determined from the normalised inclusive jet or 2-jet cross sections and 0.8% when measured with the normalised 3-jet cross sections. This uncertainty is twice as large as that estimated with the uncertainties given for the MSTW2008nlo90cl set [37] which in turn exceeds the difference between α_s values extracted with the central sets of CTEQ6.5M and MSTW2008nlo. The PDFs also depend on the value of α_s. Potential biases on the α_s extraction from that source have been studied in detail previously [3]. For this analysis, the resulting uncertainty is found to be negligible.

Individual fits of $\alpha_s(\mu_r)$ are made to each of the 24 measurements of the normalised double differential inclusive jet cross section, as shown in figure 7a. These individual determinations show the expected scale dependence. Equivalently, the α_s values at each scale μ_r can be related to the value of the strong coupling $\alpha_s(M_Z)$ at the Z^0 mass as shown in figure 8.

Then $\alpha_s(M_Z)$ is determined by a common fit to the normalised inclusive jet cross section in four P_T bins for each region in Q^2. The resulting six values are evolved from the scale M_Z to the average Q in that region (figure 10a). Finally, a central value $\alpha_s(M_Z)$ is extracted from a common fit to all 24 measurements and given in table 9. The result of evolving this value together with its associated uncertainty is also shown as the curve and surrounding band in figure 10a.

The same fit procedure of successive combination steps is applied to the 24 points of the normalised 2-jet cross section with $\langle P_T \rangle > 7$ GeV (figure 7b, 9 and 10b). The bins with $5 < \langle P_T \rangle < 7$ GeV are not used for the extraction of the strong coupling since the theory uncertainty is significantly larger than in the other bins (figure 5). The fit procedure is also applied to the 6 points of the normalised 3-jet cross section (figure 10c). The normalised 3-jet cross section (figure 3c), which is $\mathcal{O}(\alpha_s^2)$, is preferred to the ratio of the 3-jet cross section to the 2-jet cross section (figure 3d), which is $\mathcal{O}(\alpha_s^1)$, due to better sensitivity to the strong coupling. The three values of $\alpha_s(M_Z)$ determined from the normalised inclusive jet (24 points), 2-jet (24 points) and 3-jet (6 points) cross sections are given in table 9 with experimental and theoretical uncertainties. All obtained values are compatible with each other within two standard deviations of the experimental uncertainty.

The impact of the choice of renormalisation scale on the central value of $\alpha_s(M_Z)$ is studied in the case of the normalised inclusive jet cross section by repeating the fit procedure with $\mu_r = P_T$ and $\mu_r = Q$ instead of $\mu_r = \sqrt{(Q^2 + P_T^2)/2}$. In the first case the central value of the $\alpha_s(M_Z)$ is found to be approximatively 0.7% smaller and in the latter approximatively 1.5% bigger with respect to the nominal fit, a difference which is well inside the estimated theoretical uncertainties. Similar deviations are observed for the normalised 2-jet and 3-jet cross sections when $\mu_r = Q$ is used instead of $\mu_r = \sqrt{(Q^2 + P_{T,\,\mathrm{obs}}^2)/2}$. To get information on the description of the data by the NLO calculations as a function of the renormalisation scale, the χ^2 of the fit is studied in the case of the normalised inclusive jet cross section for different values of the parameter x_r, defined by $\mu_r = x_r \cdot \sqrt{(Q^2 + P_T^2)/2}$. The results are shown in figure 11, where the α_s fit is repeated for different choices of x_r and the corresponding χ^2 values are shown.

The lowest χ^2 value is obtained for $x_r \simeq 0.5$ while x_r choices above 2.0 and below 0.3 are disfavoured.

The sensitivity of the strong coupling determination procedure to the choice of the jet definition is tested for the normalised inclusive jet and 2-jet cross sections by repeating all the extraction procedure using the anti-k_T metric [38] instead of k_T, but keeping the recombination scheme and the distance parameter unchanged. The resulting central value of $\alpha_s(M_Z)$ differs in both cases by less than 0.6% from the central value extracted using the k_T metric.

In each Q^2 region the values of $\alpha_s(M_Z)$ from different observables are combined taking into account statistical and systematic correlations. The resulting values, evolved from the scale M_Z to the average μ_r of the measurements in each Q^2 region, are shown in figure 12. This visualises the running of α_s for scales between 10 and 100 GeV and the corresponding experimental and theory uncertainties. All 54 data points are used in a common fit of the strong coupling taking the correlations into account with a fit quality $\chi^2/\mathrm{ndf} = 65.0/53$ (see table 9), which is also shown in figure 12.

The values of $\alpha_s(M_Z)$ obtained in this way are also consistent with the world averages $\alpha_s(M_Z) = 0.1176 \pm 0.0020$ [39] and $\alpha_s(M_Z) = 0.1189 \pm 0.0010$ [40], and with the previous H1 and ZEUS determinations from inclusive jet production measurements [3, 4] and multijet production [41]. The experimental error on $\alpha_s(M_Z)$ measured with each observable typically amounts to 1%. The combination of different observables, even though partially correlated, gives rise to additional constraints on the strong coupling and leads to an improved experimental uncertainty of 0.6%. The experimental error on α_s is independent of the choice of renormalisation scale within the variation used to determine the theoretical uncertainty. The total error is strongly dominated by the theoretical uncertainty due to missing higher orders in the perturbative calculation which is about 4%.

5 Conclusion

Measurements of the normalised inclusive, 2-jet and 3-jet cross sections in the Breit frame in deep-inelastic electron-proton scattering in the range $150 < Q^2 < 15000\,\mathrm{GeV}^2$ and $0.2 < y < 0.7$ using the H1 data taken in years 1999 to 2007 are presented. Calculations at NLO QCD, corrected for hadronisation effects, provide a good description of the single and double differential cross sections as functions of the jet transverse momentum P_T, the boson virtuality Q^2 as well as of the proton momentum fraction ξ. The strong coupling α_s is determined from a fit of the NLO prediction to the measured normalised jet cross sections. The normalisation leads to cancellations of systematic effects, resulting in improved experimental and PDF uncertainties. The experimentally most precise determination of $\alpha_s(M_Z)$ is derived from a common fit to the normalised jet cross sections:

$$\alpha_s(M_Z) = 0.1168 \ \pm 0.0007\,(\mathrm{exp.})\,^{+0.0046}_{-0.0030}\,(\mathrm{th.})\ \pm 0.0016\,(\mathrm{PDF})\,.$$

The dominating source of the uncertainty is due to the renormalisation scale dependence, which is used to estimate the effect of missing higher orders beyond NLO in the pQCD prediction. This measurement improves the experimental precision on α_s determinations from other recent jet measurements at HERA [3,4]. The result is competitive with those from e^+e^- data [40,42] and is in good agreement with the world average [39, 40].

Acknowledgements

We are grateful to the HERA machine group whose outstanding efforts have made this experiment possible. We thank the engineers and technicians for their work in constructing and maintaining the H1 detector, our funding agencies for financial support, the DESY technical staff for continual assistance and the DESY directorate for support and for the hospitality which they extend to the non DESY members of the collaboration. Furthermore we thank Gavin Salam, Matteo Cacciari, Mrinal Dasgupta and Zoltan Nagy for fruitful discussions.

References

[1] R. P. Feynman, "Photon-Hadron Interactions", Benjamin, New York (1972).

[2] C. Adloff *et al.* [H1 Collaboration], Eur. Phys. J. C **19** (2001) 289 [hep-ex/0010054].

[3] A. Aktas *et al.* [H1 Collaboration], Phys. Lett. B **653** (2007) 134 [arXiv:0706.3722].

[4] S. Chekanov *et al.* [ZEUS Collaboration], Phys. Lett. B **649** (2007) 12 [hep-ex/0701039].

[5] I. Abt *et al.* [H1 Collaboration], Nucl. Instrum. Meth. A **386** (1997) 310, ibid., 348.

[6] R. D. Appuhn *et al.* [H1 SPACAL Group], Nucl. Instrum. Meth. A **386** (1997) 397.

[7] B. Andrieu *et al.* [H1 Calorimeter Group], Nucl. Instrum. Meth. A **336** (1993) 460.

[8] B. Andrieu *et al.* [H1 Calorimeter Group], Nucl. Instrum. Meth. A **336** (1993) 499;
B. Andrieu *et al.* [H1 Calorimeter Group], Nucl. Instrum. Meth. A **350** (1994) 57.

[9] D. Pitzl *et al.*, Nucl. Instrum. Meth. A **454** (2000) 334 [hep-ex/0002044];
B. List *et al.*, Nucl. Instrum. Meth. A **549** (2005) 33.

[10] C. Adloff *et al.* [H1 Collaboration], Eur. Phys. J. C **30** (2003) 1 [hep-ex/0304003].

[11] M. Peez, "Search for deviations from the standard model in high transverse energy processes at the electron proton collider HERA" (in French), CPPM-T-2003-04 (available at http://www-h1.desy.de/psfiles/theses/).

[12] B. Portheault, "First measurement of charged and neutral current cross sections with the polarized positron beam at HERA II and QCD-electroweak analyses" (in French), LAL-05-05 (available at http://www-h1.desy.de/psfiles/theses/).

[13] U. Bassler and G. Bernardi, Nucl. Instrum. Meth. A **361** (1995) 197 [hep-ex/9412004];
U. Bassler and G. Bernardi, Nucl. Instrum. Meth. A **426** (1999) 583 [hep-ex/9801017].

[14] S. D. Ellis and D. E. Soper, Phys. Rev. D **48** (1993) 3160 [hep-ph/9305266];
S. Catani *et al.*, Nucl. Phys. B **406** (1993) 187.

[15] S. Frixione and G. Ridolfi, Nucl. Phys. B **507** (1997) 315 [hep-ph/9707345].

[16] K. Charchula, G. A. Schuler and H. Spiesberger, DJANGOH 1.4, Comput. Phys. Commun. **81** (1994) 381.

[17] L. Lönnblad, ARIADNE 4.08, Comput. Phys. Commun. **71** (1992) 15.

[18] H. Jung, RAPGAP 2.08, Comput. Phys. Commun. **86** (1995) 147.

[19] B. Andersson, G. Gustafson, G. Ingelman and T. Sjostrand, JETSET 7.41, Phys. Rept. **97** (1983) 31.

[20] R. Brun *et al.*, "GEANT3", CERN-DD/EE/84-1.

[21] M. Gouzevitch, "Measurement of the strong coupling constant alpha(s) with hadronic jets in Deep Inelastic Scattering" (in French), DESY-THESIS-2008-047 (available at http://www-h1.desy.de/psfiles/theses/).

[22] A. Kwiatkowski, H. Spiesberger and H. J. Möhring, HERACLES 4.63, Comput. Phys. Commun. **69** (1992) 155.

[23] G. Ingelman, A. Edin and J. Rathsman, LEPTO 6.5, Comput. Phys. Commun. **101** (1997) 108 [hep-ph/9605286].

[24] B.R. Webber, J. Phys. **G19** (1993) 1567.

[25] Z. Nagy and Z. Trocsanyi, NLOJET++ 4.0.1, Phys. Rev. Lett. **87** (2001) 082001 [hep-ph/0104315].

[26] S. Catani and M. H. Seymour, Nucl. Phys. B **485** (1997) 291 [Erratum-ibid. B **510** (1998) 503] [hep-ph/9605323].

[27] T. Kluge, K. Rabbertz and M. Wobisch, FastNLO 1.0, hep-ph/0609285, published in "Deep inelastic scattering DIS2006, Proceedings of the 14th workshop", eds. M. Kuze, K. Nagano, K. Tokushuka, 483.

[28] W. K. Tung *et al.* JHEP **0702** (2007) 053 [hep-ph/0611254].

[29] M. Dasgupta and Y. Delenda, JHEP **0907** (2009) 004 [arXiv:0903.2187];
M. Dasgupta, L. Magnea and G. P. Salam, JHEP **0802** (2008) 055 [arXiv:0712.3014];
M. Dasgupta and B. R. Webber, Eur. Phys. J. C **1** (1998) 539 [hep-ph/9704297];
M. Dasgupta and B. R. Webber, JHEP **9810** (1998) 001 [hep-ph/9809247].

[30] Y. L. Dokshitzer, G. Marchesini and B. R. Webber, Nucl. Phys. B **469** (1996) 93 [hep-ph/9512336].

[31] A. Aktas *et al.* [H1 Collaboration], Eur. Phys. J. C **46** (2006) 343 [hep-ex/0512014].

[32] C. Pascaud and F. Zomer, preprint LAL 95-05 (1995).

[33] M. Botje, Eur. Phys. J. C **14** (2000) 285 [hep-ph/9912439].

[34] V. Barone, C. Pascaud and F. Zomer, Eur. Phys. J. C **12** (2000) 243 [hep-ph/9907512].

[35] C. Adloff *et al.* [H1 Collaboration], Phys. Lett. B **479** (2000) 358 [hep-ex/0003002].

[36] R. W. L. Jones *et al.*, JHEP **0312** (2003) 007 [hep-ph/0312016].

[37] A. D. Martin, W. J. Stirling, R. S. Thorne and G. Watt, arXiv:0901.0002.

[38] M. Cacciari, G. P. Salam and G. Soyez, JHEP **0804** (2008) 063 [arXiv:0802.1189].

[39] C. Amsler *et al.* [Particle Data Group], Phys. Lett. B **667** (2008) 1.

[40] S. Bethke, Prog. Part. Nucl. Phys. **58** (2007) 351 [hep-ex/0606035].

[41] S. Chekanov *et al.* [ZEUS Collaboration], Eur. Phys. J. C **44** (2005) 183 [hep-ex/0502007].

[42] G. Dissertori *et al.*, JHEP **0802** (2008) 040 [arXiv:0712.0327].

NC DIS Selection	$150 < Q^2 < 15000$ GeV^2 $\quad 0.2 < y < 0.7$		
Inclusive jet	$7 < P_T < 50$ GeV		$-0.8 < \eta^{\rm jet}_{\rm Lab} < 2.0$
2-jet	$5 < P_T^{\rm jet\,1},\ P_T^{\rm jet\,2} < 50$ GeV	$M_{12} > 16$ GeV	
3-jet	$5 < P_T^{\rm jet\,1},\ P_T^{\rm jet\,2},\ P_T^{\rm jet\,3} < 50$ GeV		

Table 1: Selection criteria for the NC DIS and jet samples.

bin number	corresponding Q^2 range
1	$150 \le Q^2 < 200\,\mathrm{GeV}^2$
2	$200 \le Q^2 < 270\,\mathrm{GeV}^2$
3	$270 \le Q^2 < 400\,\mathrm{GeV}^2$
4	$400 \le Q^2 < 700\,\mathrm{GeV}^2$
5	$700 \le Q^2 < 5000\,\mathrm{GeV}^2$
6	$5000 \le Q^2 < 15000\,\mathrm{GeV}^2$

bin letter	corresponding P_T or $\langle P_T \rangle$ range
a'	$5 \le P_T < 7$ GeV
a	$7 \le P_T < 11$ GeV
b	$11 \le P_T < 18$ GeV
c	$18 \le P_T < 30$ GeV
d	$30 \le P_T < 50$ GeV

bin letter	corresponding ξ range
A	$0.006 \le \xi < 0.020$
B	$0.020 \le \xi < 0.040$
C	$0.040 \le \xi < 0.080$
D	$0.080 \le \xi < 0.316$

Table 2: Nomenclature for the bins in Q^2, P_T for the inclusive jet or $\langle P_T \rangle$ for 2-jets and ξ used in the following tables. In case of the normalised 2-jet cross section, the bin a' in $\langle P_T \rangle$ is not used for the α_s extraction.

Normalised inclusive jet cross section in bins of Q^2

bin	normalised cross section	statistical uncert. (%)	total uncert. (%)	total uncorrelated uncertainty (%)	total correlated uncert. (%)	single contributions to correlated uncertainty: electron energy scale (%)	electron polar angle (%)	hadronic energy scale (%)	hadronisation correction factor	hadronisation correction uncertainty (%)
1	$2.39\,10^{-1}$	0.7	3.2	2.4	2.1	0.6	0.8	1.9	0.95	0.6
2	$2.69\,10^{-1}$	0.7	3.0	2.2	1.9	0.6	0.6	1.7	0.94	0.6
3	$3.11\,10^{-1}$	0.8	2.9	2.3	1.8	0.6	0.4	1.6	0.94	0.8
4	$3.62\,10^{-1}$	0.8	2.7	2.2	1.7	0.7	0.3	1.5	0.94	0.6
5	$4.26\,10^{-1}$	0.9	2.7	2.3	1.6	0.9	0.1	1.3	0.93	1.7
6	$5.02\,10^{-1}$	3.2	5.7	5.2	2.4	2.2	0.3	0.8	0.93	3.0

Normalised 2-jet cross section in bins of Q^2

1	$8.81\,10^{-2}$	1.0	2.9	2.2	1.9	0.4	0.7	1.7	0.94	1.1
2	$1.01\,10^{-1}$	1.1	2.6	2.1	1.7	0.3	0.6	1.5	0.93	1.3
3	$1.19\,10^{-1}$	1.1	2.4	1.9	1.5	0.2	0.4	1.4	0.93	1.3
4	$1.41\,10^{-1}$	1.2	2.5	2.0	1.4	0.3	0.4	1.3	0.91	1.1
5	$1.75\,10^{-1}$	1.2	2.4	2.1	1.2	0.1	0.2	1.1	0.91	2.9
6	$1.97\,10^{-1}$	4.4	7.7	7.6	1.1	0.3	0.2	1.0	0.91	2.9

Normalised 3-jet cross section in bins of Q^2

1	$1.19\,10^{-2}$	2.6	5.1	4.1	3.1	0.4	1.3	2.8	0.85	2.4
2	$1.29\,10^{-2}$	2.8	5.1	4.2	2.9	0.3	0.7	2.8	0.84	1.7
3	$1.68\,10^{-2}$	2.7	4.6	3.8	2.6	0.1	0.9	2.5	0.83	1.0
4	$2.06\,10^{-2}$	2.9	4.7	4.0	2.5	0.3	0.8	2.4	0.82	0.6
5	$2.36\,10^{-2}$	2.8	6.6	6.2	2.3	0.4	0.4	2.2	0.81	1.2
6	$2.82\,10^{-2}$	9.2	18.7	18.5	2.3	0.4	0.3	2.3	0.75	3.6

3-jet cross section normalised to 2-jet cross section in bins of Q^2

1	$1.36\,10^{-1}$	2.7	4.4	4.3	1.2	0.2	0.5	1.1	0.91	1.5
2	$1.28\,10^{-1}$	3.0	4.7	4.5	1.4	0.5	0.1	1.3	0.90	1.0
3	$1.41\,10^{-1}$	2.9	4.5	4.3	1.1	0.2	0.1	1.1	0.90	0.9
4	$1.46\,10^{-1}$	3.1	4.8	4.6	1.2	0.7	0.3	1.0	0.90	0.6
5	$1.35\,10^{-1}$	3.0	5.1	5.0	1.2	0.4	0.2	1.1	0.89	1.5
6	$1.43\,10^{-1}$	9.8	14.2	14.1	1.3	0.3	0.2	1.2	0.82	3.3

Table 3: Normalised inclusive jet, 2-jet and 3-jet cross sections in NC DIS measured as a function of Q^2. The measurements refer to the phase-space defined in table 1. In columns 3 to 9 are shown the statistical uncertainty, the total experimental uncertainty, the total uncorrelated uncertainty including the statistical one and the total correlated uncertainty calculated as the quadratic sum of the following three components: the electron energy scale, the electron polar angle uncertainty and the hadron energy scale uncertainty. The sharing of the uncertainties between correlated and uncorrelated sources is described in detail in section 4.2. The hadronisation correction factors applied to the NLO predictions and their uncertainties are shown in columns 10 and 11. The bin nomenclature of column 1 is defined in table 2.

Normalised inclusive jet cross section in bins of Q^2 and P_T

bin	normalised cross section	statistical uncert. (%)	total uncert. (%)	total uncorrelated uncertainty (%)	total correlated uncert. (%)	single contributions to correlated uncertainty: electron energy scale (%)	electron polar angle (%)	hadronic energy scale (%)	hadronisation correction factor	hadronisation correction uncertainty (%)
1 a	$1.53\,10^{-1}$	0.8	2.7	2.1	1.7	0.6	0.6	1.4	0.94	0.7
1 b	$6.93\,10^{-2}$	1.2	4.5	3.5	2.9	0.6	1.1	2.6	0.97	0.3
1 c	$1.53\,10^{-2}$	2.5	6.1	4.7	3.9	0.6	1.6	3.5	0.96	0.6
1 d	$1.93\,10^{-3}$	7.2	10.6	9.7	4.4	0.2	1.3	4.2	0.95	1.8
2 a	$1.66\,10^{-1}$	0.9	2.6	2.2	1.4	0.7	0.4	1.2	0.93	0.6
2 b	$8.10\,10^{-2}$	1.3	3.9	3.0	2.5	0.6	0.8	2.3	0.97	0.4
2 c	$1.97\,10^{-2}$	2.6	5.8	4.6	3.6	0.3	0.9	3.5	0.96	0.9
2 d	$2.67\,10^{-3}$	7.1	10.2	9.1	4.6	0.4	0.5	4.5	0.97	3.2
3 a	$1.82\,10^{-1}$	1.0	2.8	2.4	1.4	0.7	0.4	1.1	0.92	0.7
3 b	$9.82\,10^{-2}$	1.3	3.5	2.7	2.2	0.5	0.4	2.1	0.97	1.0
3 c	$2.76\,10^{-2}$	2.4	5.5	4.4	3.3	0.3	0.8	3.2	0.96	0.4
3 d	$3.11\,10^{-3}$	7.0	9.8	8.5	4.8	0.1	1.9	4.4	0.95	3.2
4 a	$2.02\,10^{-1}$	1.1	2.4	2.2	1.1	0.7	0.2	0.9	0.92	0.5
4 b	$1.16\,10^{-1}$	1.3	3.4	2.8	2.0	0.8	0.4	1.8	0.96	0.5
4 c	$3.83\,10^{-2}$	2.3	5.9	4.9	3.3	0.5	0.7	3.1	0.97	1.5
4 d	$5.28\,10^{-3}$	6.3	8.9	7.9	4.1	0.3	0.6	4.1	0.96	2.7
5 a	$2.13\,10^{-1}$	1.2	2.4	2.1	1.1	0.8	0.1	0.7	0.90	2.4
5 b	$1.42\,10^{-1}$	1.3	3.3	2.8	1.7	0.9	0.1	1.5	0.96	1.1
5 c	$5.91\,10^{-2}$	2.0	4.7	3.8	2.7	0.9	0.1	2.6	0.97	0.3
5 d	$1.09\,10^{-2}$	4.4	7.4	6.3	3.9	0.1	0.3	3.8	0.96	3.1
6 a	$2.32\,10^{-1}$	4.3	8.1	7.8	2.3	2.2	0.4	0.4	0.90	3.9
6 b	$1.62\,10^{-1}$	4.8	7.5	6.9	2.9	2.8	0.4	0.7	0.94	2.5
6 c	$8.14\,10^{-2}$	6.7	9.8	9.4	2.6	2.2	0.1	1.4	0.96	0.8
6 d	$2.66\,10^{-2}$	9.7	19.0	18.8	3.1	0.6	0.5	3.0	0.97	3.6

Table 4: Normalised inclusive jet cross sections as a function of Q^2 and P_T together with their relative errors and hadronisation correction factors. Other details are given in the caption to table 3. The bin nomenclature is defined in table 2.

Normalised 2-jet cross section in bins of Q^2 and $\langle P_T \rangle$

bin	normalised cross section	statistical uncert. (%)	total uncert. (%)	total uncorrelated uncertainty (%)	total correlated uncert. (%)	single contributions to correlated uncertainty: electron energy scale (%)	electron polar angle (%)	hadronic energy scale (%)	hadronisation correction factor	hadronisation correction uncertainty (%)
1 a'	$9.14\,10^{-3}$	3.2	3.5	3.5	0.6	0.5	0.1	0.3	0.83	2.5
1 a	$4.40\,10^{-2}$	1.4	2.9	2.6	1.4	0.5	0.5	1.2	0.94	1.4
1 b	$2.77\,10^{-2}$	1.7	4.4	3.6	2.6	0.4	1.0	2.3	0.96	1.4
1 c	$6.28\,10^{-3}$	3.5	6.8	5.3	4.2	0.3	1.9	3.8	0.96	1.4
1 d	$6.87\,10^{-4}$	10.5	12.6	11.7	4.5	0.1	0.8	4.5	0.95	1.8
2 a'	$1.04\,10^{-2}$	3.5	4.2	4.1	0.9	0.2	0.8	0.2	0.83	1.1
2 a	$4.91\,10^{-2}$	1.5	2.8	2.5	1.2	0.4	0.5	1.0	0.94	1.3
2 b	$3.26\,10^{-2}$	1.8	3.8	3.0	2.2	0.4	0.8	2.1	0.96	1.9
2 c	$7.80\,10^{-3}$	3.6	6.3	5.1	3.6	0.2	1.1	3.4	0.96	1.7
2 d	$1.05\,10^{-3}$	10.1	12.5	11.5	4.9	0.4	0.5	4.8	0.92	3.3
3 a'	$1.13\,10^{-2}$	3.7	3.9	3.9	0.3	0.3	0.1	0.2	0.80	1.4
3 a	$5.56\,10^{-2}$	1.6	2.6	2.4	0.9	0.3	0.3	0.8	0.92	0.3
3 b	$3.99\,10^{-2}$	1.8	3.4	2.9	1.9	0.4	0.3	1.8	0.97	2.2
3 c	$1.10\,10^{-2}$	3.3	5.9	4.8	3.3	0.1	0.8	3.2	0.96	1.0
3 d	$1.16\,10^{-3}$	10.1	13.2	11.8	5.9	0.2	2.9	5.2	0.94	2.7
4 a'	$1.41\,10^{-2}$	3.9	4.1	4.1	0.2	0.1	0.1	0.2	0.79	2.7
4 a	$6.13\,10^{-2}$	1.8	2.7	2.6	0.8	0.3	0.1	0.7	0.90	0.1
4 b	$4.80\,10^{-2}$	1.9	3.5	2.9	1.8	0.6	0.5	1.7	0.96	1.3
4 c	$1.57\,10^{-2}$	3.2	6.3	5.6	3.0	0.2	0.6	2.9	0.97	1.2
4 d	$2.09\,10^{-3}$	9.1	12.7	11.8	4.7	0.1	0.7	4.7	0.96	2.6
5 a'	$1.53\,10^{-2}$	4.2	9.2	9.2	0.8	0.7	0.2	0.0	0.77	2.3
5 a	$6.95\,10^{-2}$	1.9	2.6	2.5	0.5	0.1	0.2	0.5	0.89	3.6
5 b	$5.98\,10^{-2}$	1.9	2.9	2.6	1.3	0.3	0.1	1.3	0.94	1.1
5 c	$2.49\,10^{-2}$	2.8	4.7	4.0	2.5	0.1	0.5	2.4	0.97	2.2
5 d	$4.34\,10^{-3}$	6.4	9.1	8.1	4.2	0.4	0.7	4.1	0.96	2.5
6 a'	$1.30\,10^{-2}$	16.2	36.2	36.1	2.4	2.3	0.6	0.6	0.73	16.2
6 a	$7.47\,10^{-2}$	7.1	10.6	10.6	0.5	0.4	0.1	0.3	0.88	1.0
6 b	$6.42\,10^{-2}$	6.9	8.0	7.8	1.5	0.9	0.3	1.1	0.93	4.4
6 c	$3.36\,10^{-2}$	9.2	9.7	9.5	1.6	0.7	0.4	1.3	0.95	1.8
6 d	$1.03\,10^{-2}$	15.7	19.2	18.8	3.6	0.6	0.5	3.5	0.97	4.3

Table 5: Normalised 2-jet cross sections as a function of Q^2 and $\langle P_T \rangle$ together with their relative errors and hadronisation correction factors. Other details are given in the caption to table 3. The bin nomenclature is defined in table 2.

Normalised 2-jet cross section in bins of Q^2 and ξ

bin	normalised cross section	statistical uncert. (%)	total uncert. (%)	total uncorrelated uncertainty (%)	total correlated uncert. (%)	single contributions to correlated uncertainty: electron energy scale (%)	electron polar angle (%)	hadronic energy scale (%)	hadronisation correction factor	hadronisation correction uncertainty (%)
1 A	$4.36\,10^{-2}$	1.4	2.5	2.1	1.3	0.7	0.5	1.0	0.95	0.7
1 B	$3.37\,10^{-2}$	1.6	3.6	2.9	2.1	0.4	0.8	1.9	0.93	1.7
1 C	$9.22\,10^{-3}$	2.9	6.1	4.8	3.8	0.4	1.6	3.4	0.92	3.2
1 D	$1.88\,10^{-3}$	6.5	10.5	8.8	5.6	1.2	2.4	4.9	0.91	1.3
2 A	$4.20\,10^{-2}$	1.7	2.8	2.5	1.3	0.9	0.6	0.7	0.95	0.6
2 B	$4.44\,10^{-2}$	1.6	2.8	2.3	1.7	0.2	0.6	1.6	0.93	2.7
2 C	$1.26\,10^{-2}$	2.8	5.5	4.4	3.3	0.7	1.0	3.1	0.93	1.3
2 D	$2.48\,10^{-3}$	6.3	10.6	9.1	5.4	2.1	1.0	4.9	0.91	1.5
3 A	$3.82\,10^{-2}$	2.0	3.1	2.8	1.2	1.1	0.3	0.4	0.93	1.1
3 B	$5.86\,10^{-2}$	1.5	2.4	2.1	1.3	0.2	0.4	1.2	0.92	1.2
3 B	$1.93\,10^{-2}$	2.5	4.9	3.9	2.9	0.5	0.6	2.8	0.93	1.8
3 D	$3.78\,10^{-3}$	5.6	9.1	7.7	4.9	1.0	1.8	4.5	0.91	2.9
4 A	$2.36\,10^{-2}$	2.9	4.2	4.0	1.4	1.3	0.1	0.3	0.92	1.2
4 B	$7.22\,10^{-2}$	1.6	2.5	2.2	1.2	0.5	0.4	1.1	0.91	1.7
4 C	$3.91\,10^{-2}$	2.1	3.6	3.0	2.0	0.5	0.4	1.9	0.91	0.9
4 D	$7.01\,10^{-3}$	4.8	8.0	6.9	4.2	1.2	1.0	3.9	0.93	3.4
5 A	$2.91\,10^{-3}$	8.7	8.9	8.8	1.1	0.6	0.8	0.5	0.92	3.2
5 B	$4.50\,10^{-2}$	2.3	2.9	2.7	0.9	0.8	0.3	0.5	0.91	3.2
5 C	$8.09\,10^{-2}$	1.7	2.5	2.2	1.1	0.1	0.2	1.1	0.91	2.6
5 D	$4.54\,10^{-2}$	2.1	4.7	4.2	2.2	0.7	0.7	1.9	0.90	2.9
6 A	—	—	—	—	—	—	—	—	—	—
6 B	—	—	—	—	—	—	—	—	—	—
6 C	—	—	—	—	—	—	—	—	—	—
6 D	$1.80\,10^{-1}$	4.6	7.6	7.5	1.5	1.0	0.3	1.1	0.91	3.3

Table 6: Normalised 2-jet cross sections as a function of Q^2 and ξ together with their relative errors and hadronisation correction factors. Other details are given in the caption to table 3. The bin nomenclature is defined in table 2. At high Q^2 small ξ values are kinematically disfavoured or forbidden.

$150 < Q^2 < 200\,\mathrm{GeV}^2$		jet				2-jet				3-jet
		1 a	1 b	1 c	1 d	1 a	1 b	1 c	1 d	1
jet	1 a	100	16	5	1	59	19	2	0	26
	1 b	16	100	12	2	22	72	12	1	30
	1 c	5	12	100	8	0	19	77	6	19
	1 d	1	2	8	100	0	0	16	78	6
2-jet	1 a	59	22	0	0	100	0	0	0	21
	1 b	19	72	19	0	0	100	0	0	30
	1 c	2	12	77	16	0	0	100	0	16
	1 d	0	1	6	78	0	0	0	100	4
3-jet	1	26	30	19	6	21	30	16	4	100

$200 < Q^2 < 270\,\mathrm{GeV}^2$		jet				2-jet				3-jet
		2 a	2 b	2 c	2 d	2 a	2 b	2 c	2 d	2
jet	2 a	100	16	4	1	58	19	2	1	25
	2 b	16	100	13	2	22	71	13	1	29
	2 c	4	13	100	9	0	20	76	8	20
	2 d	1	2	9	100	0	0	14	75	8
2-jet	2 a	58	22	0	0	100	0	0	0	21
	2 b	19	71	20	0	0	100	0	0	28
	2 c	2	13	76	14	0	0	100	0	17
	2 d	1	1	8	75	0	0	0	100	6
3-jet	2	25	29	20	8	21	28	17	6	100

$270 < Q^2 < 400\,\mathrm{GeV}^2$		jet				2-jet				3-jet
		3 a	3 b	3 c	3 d	3 a	3 b	3 c	3 d	3
jet	3 a	100	16	5	1	59	19	3	0	27
	3 b	16	100	13	2	20	71	12	1	30
	3 c	5	13	100	8	0	20	77	7	21
	3 d	1	2	8	100	0	0	16	77	8
2-jet	3 a	59	20	0	0	100	0	0	0	21
	3 b	19	71	20	0	0	100	0	0	30
	3 c	3	12	77	16	0	0	100	0	20
	3 d	0	1	7	77	0	0	0	100	6
3-jet	3	27	30	21	8	21	30	20	6	100

Table 7: The statistical correlation factors given in percent between different $P_{T,\mathrm{obs}}$ bins of different jet observables inside Q^2 bins 1 to 3 as estimated from the data. The bin nomenclature is defined in table 2.

$400 < Q^2 < 700\,\mathrm{GeV}^2$		jet				2-jet				3-jet
		4 a	4 b	4 c	4 d	4 a	4 b	4 c	4 d	4
jet	4 a	100	15	6	1	58	20	3	1	28
	4 b	15	100	13	2	19	70	14	1	31
	4 c	6	13	100	9	0	21	76	7	23
	4 d	1	2	9	100	0	0	15	78	8
2-jet	4 a	58	19	0	0	100	0	0	0	23
	4 b	20	70	21	0	0	100	0	0	30
	4 c	3	14	76	15	0	0	100	0	20
	4 d	1	1	7	78	0	0	0	100	7
3-jet	4	28	31	23	8	23	30	20	7	100

$700 < Q^2 < 5000\,\mathrm{GeV}^2$		jet				2-jet				3-jet
		5 a	5 b	5 c	5 d	5 a	5 b	5 c	5 d	5
jet	5 a	100	16	5	3	57	21	5	1	28
	5 b	16	100	13	2	20	68	14	1	30
	5 c	5	13	100	9	0	20	71	9	21
	5 d	3	2	9	100	0	0	23	72	7
2-jet	5 a	57	20	0	0	100	0	0	0	18
	5 b	21	68	20	0	0	100	0	0	29
	5 c	5	14	71	23	0	0	100	0	19
	5 d	1	1	9	72	0	0	0	100	7
3-jet	5	28	30	21	7	18	29	19	7	100

$5000 < Q^2 < 15000\,\mathrm{GeV}^2$		jet				2-jet				3-jet
		6 a	6 b	6 c	6 d	6 a	6 b	6 c	6 d	6
jet	6 a	100	16	6	3	53	22	7	0	28
	6 b	16	100	12	3	20	62	15	2	32
	6 c	6	12	100	7	0	21	58	9	22
	6 d	3	3	7	100	0	0	22	67	14
2-jet	6 a	53	20	0	0	100	0	0	0	19
	6 b	22	62	21	0	0	100	0	0	28
	6 c	7	15	58	22	0	0	100	0	25
	6 d	0	2	9	67	0	0	0	100	13
3-jet	6	28	32	22	14	19	28	25	13	100

Table 8: The statistical correlation factors given in percent between different $P_{T,\mathrm{obs}}$ bins of different jet observables inside Q^2 bins 4 to 6 as estimated from the data. The bin nomenclature is defined in table 2.

Measurement	$\alpha_S(M_Z)$	Uncertainty			χ^2/ndf
		experimental	theory	PDF	
$\frac{\sigma_{\rm jet}}{\sigma_{\rm NC}}\,(Q^2, P_T)$	0.1195	0.0010	$^{+0.0049}_{-0.0036}$	0.0018	24.7/23
$\frac{\sigma_{\text{2-jet}}}{\sigma_{\rm NC}}\,(Q^2, \langle P_T \rangle)$	0.1155	0.0009	$^{+0.0042}_{-0.0031}$	0.0017	30.4/23
$\frac{\sigma_{\text{3-jet}}}{\sigma_{\rm NC}}\,(Q^2)$	0.1172	0.0013	$^{+0.0052}_{-0.0031}$	0.0009	7.0/5
$\frac{\sigma_{\rm jet}}{\sigma_{\rm NC}}$, $\frac{\sigma_{\text{2-jet}}}{\sigma_{\rm NC}}$, $\frac{\sigma_{\text{3-jet}}}{\sigma_{\rm NC}}$	0.1168	0.0007	$^{+0.0046}_{-0.0030}$	0.0016	65.0/53

Table 9: Values of $\alpha_s(M_Z)$ obtained from fits to the individual normalised inclusive jet, 2-jet and 3-jet cross sections and from a simultaneous fit to all of them. Fitted values are given with experimental, theoretical and PDF errors as well as with the normalised χ^2 of the fit.

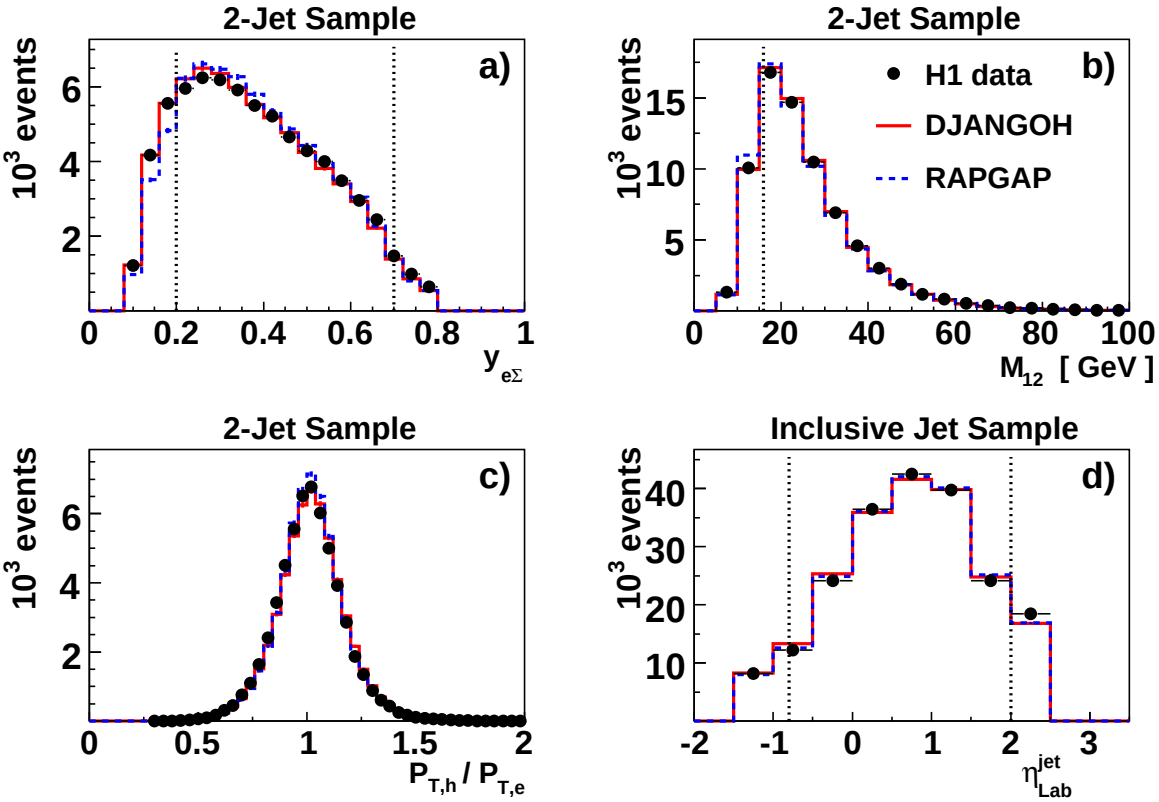

Figure 2: Distribution of the selected events (solid dots) shown as a function of selection variables in an extended domain: the inelasticity y reconstructed with the electron-Σ method of 2-jet events (a); the invariant mass of the two leading jets M_{12} (b); the transverse momentum ratio in the laboratory frame $P_{T,h}/P_{T,e}$ of 2-jet events (c); the $\eta^{\rm jet}_{\rm Lab}$ of the inclusive jets (d). The data are compared with weighted MC simulations, DJANGOH (solid line) and RAPGAP (dashed line). Vertical dashed lines indicate the positions of kinematical cuts.

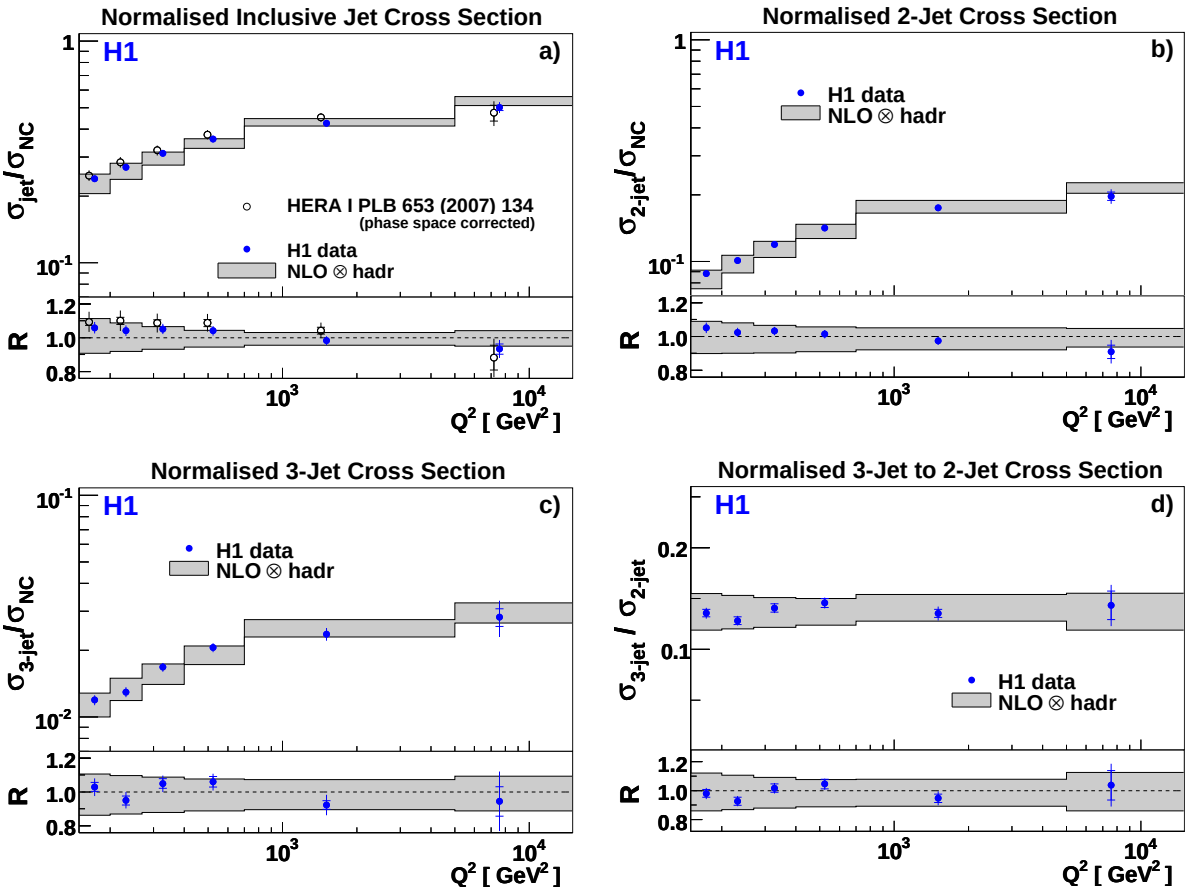

Figure 3: The normalised inclusive jet (a), 2-jet (b) and 3-jet (c) cross sections in NC DIS measured as a function of Q^2. The ratio of 3-jet to 2-jet cross sections is shown in (d). The measurements refer to the phase-space given in table 1. The points are shown at the average value of Q^2 within each bin. For the inclusive jets the present data (solid dots) are compared to HERA-I published data [3], here shown corrected to the same phase space as the present measurement and shifted in Q^2 for clarity (open dots). The inner error bars represent the statistic uncertainties. The outer error bars show the total experimental uncertainties, defined as the quadratic sum of the statistical and systematic uncertainties. The NLO QCD predictions, with parameters described in the section 3 and corrected for hadronisation effects are shown together with the theory uncertainties associated with the renormalisation and factorisation scales, the PDF and the hadronisation (grey band). The ratio R of data with respect to the NLO QCD prediction is shown in the lower part of each plot.

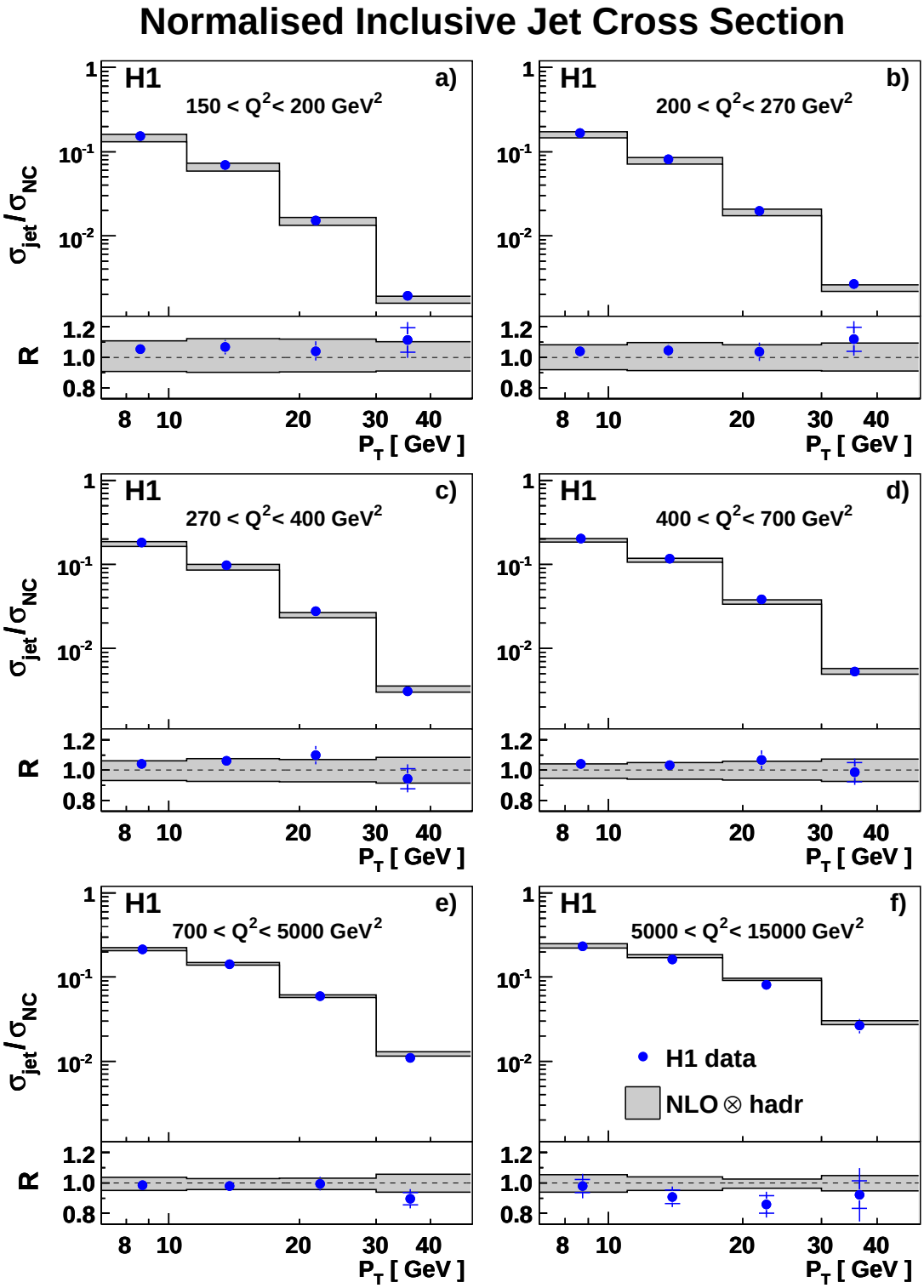

Figure 4: The normalised inclusive jet cross sections measured as a function of the jet transverse momentum in the Breit frame P_T in regions of Q^2. The points are shown at the average value of P_T within each bin. Other details are given in the caption to figure 3.

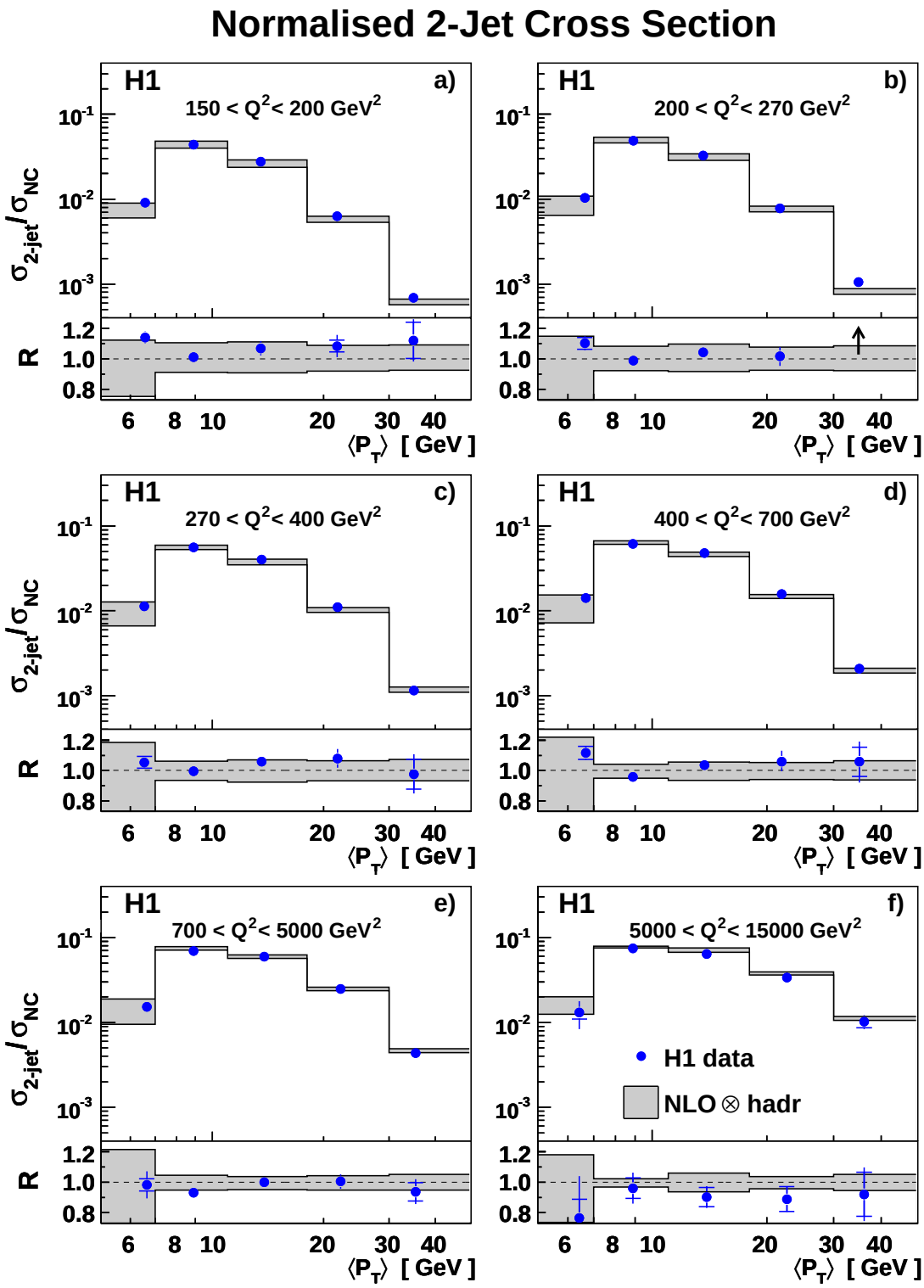

Figure 5: The normalised 2-jet cross sections measured as a function of the average transverse momentum of the two leading jets in the Breit frame $\langle P_T \rangle$ in regions of Q^2. The points are shown at the average value of $\langle P_T \rangle$ within each bin. Other details are given in the caption to figure 3.

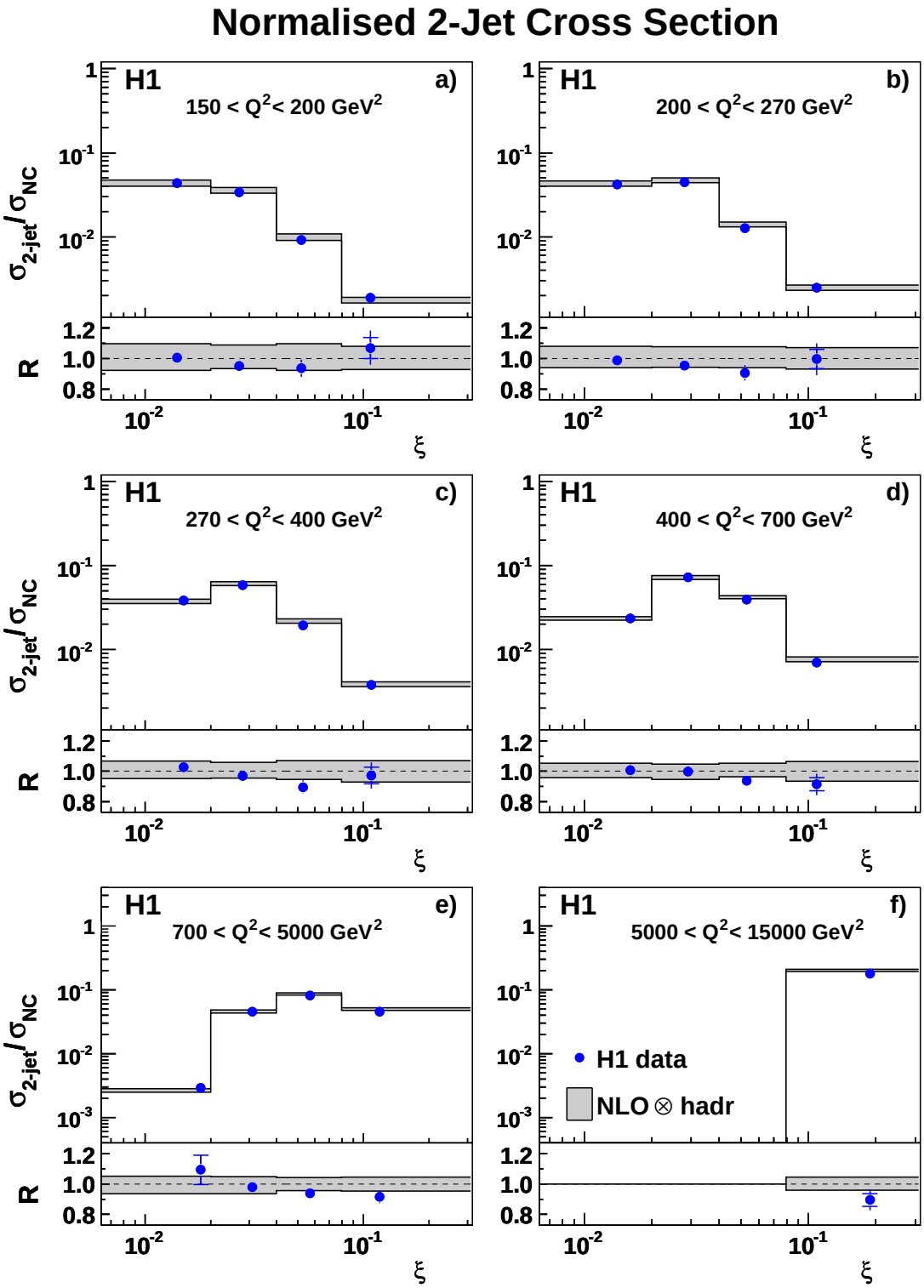

Figure 6: The normalised 2-jet cross sections measured as a function of the proton momentum fraction ξ in regions of Q^2. The points are shown at the average value of ξ within each bin. Other details are given in the caption to figure 3.

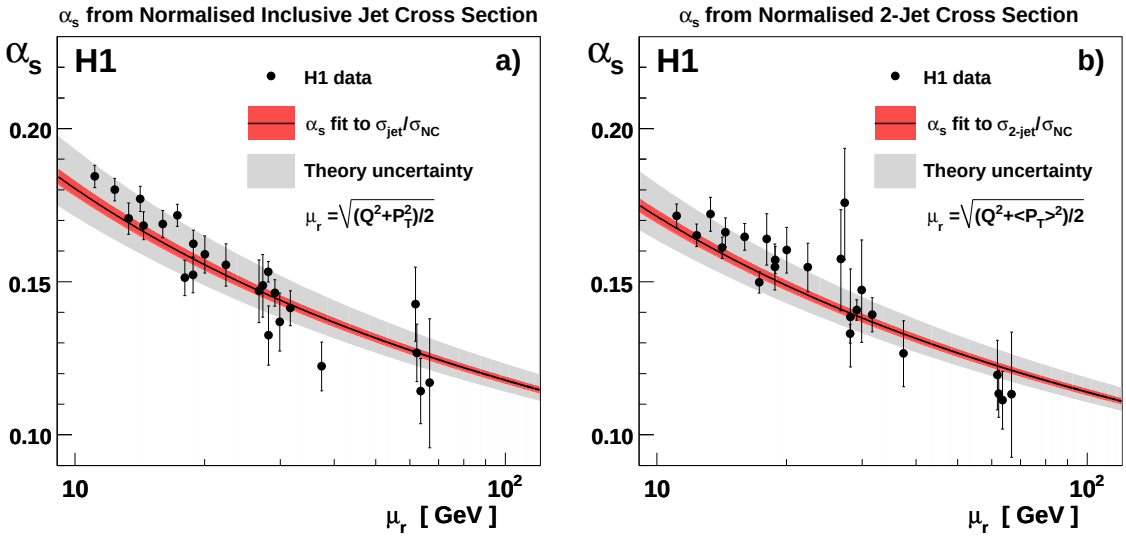

Figure 7: The $\alpha_s(\mu_r = \sqrt{(Q^2 + P_T^2)/2})$ values determined using the normalised inclusive jet cross sections (a) and the 2-jet cross sections (b), each measured in 24 bins of Q^2 and P_T. The error bars denote the total experimental uncertainty of each data point. In each plot, the solid line shows the two loop solution of the renormalisation group equation, resulting from evolving the $\alpha_s(M_Z)$ obtained from a simultaneous fit of all 24 measurements. The inner band denotes the experimental uncertainties and the outer band denotes the theoretical uncertainties associated with the renormalisation and factorisation scales, the PDF uncertainty and the model dependence of the hadronisation corrections.

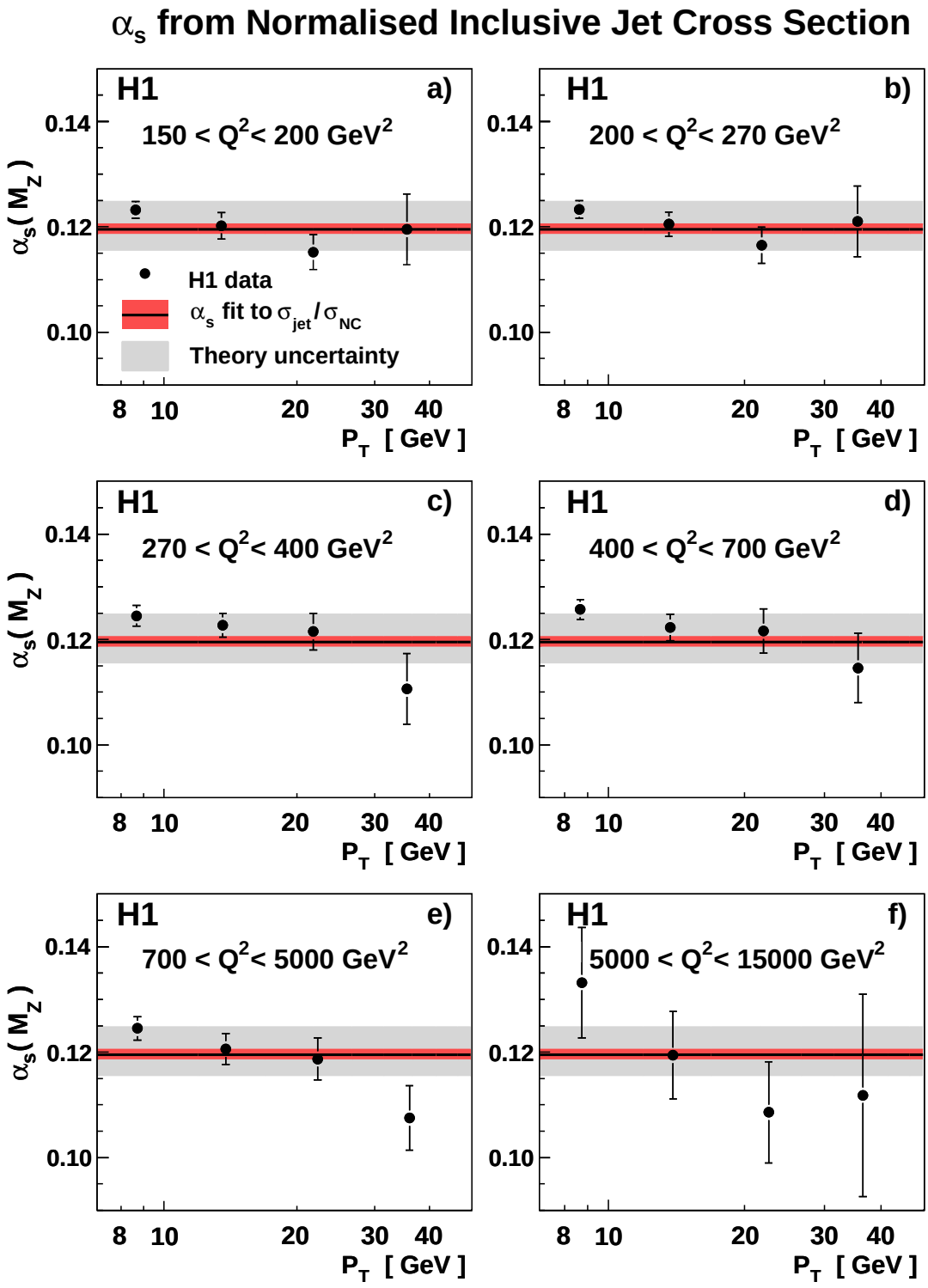

Figure 8: The $\alpha_s(M_Z)$ values determined using the normalised inclusive jet cross sections measured in 24 bins in Q^2 and P_T. Other details are given in the caption to figure 7.

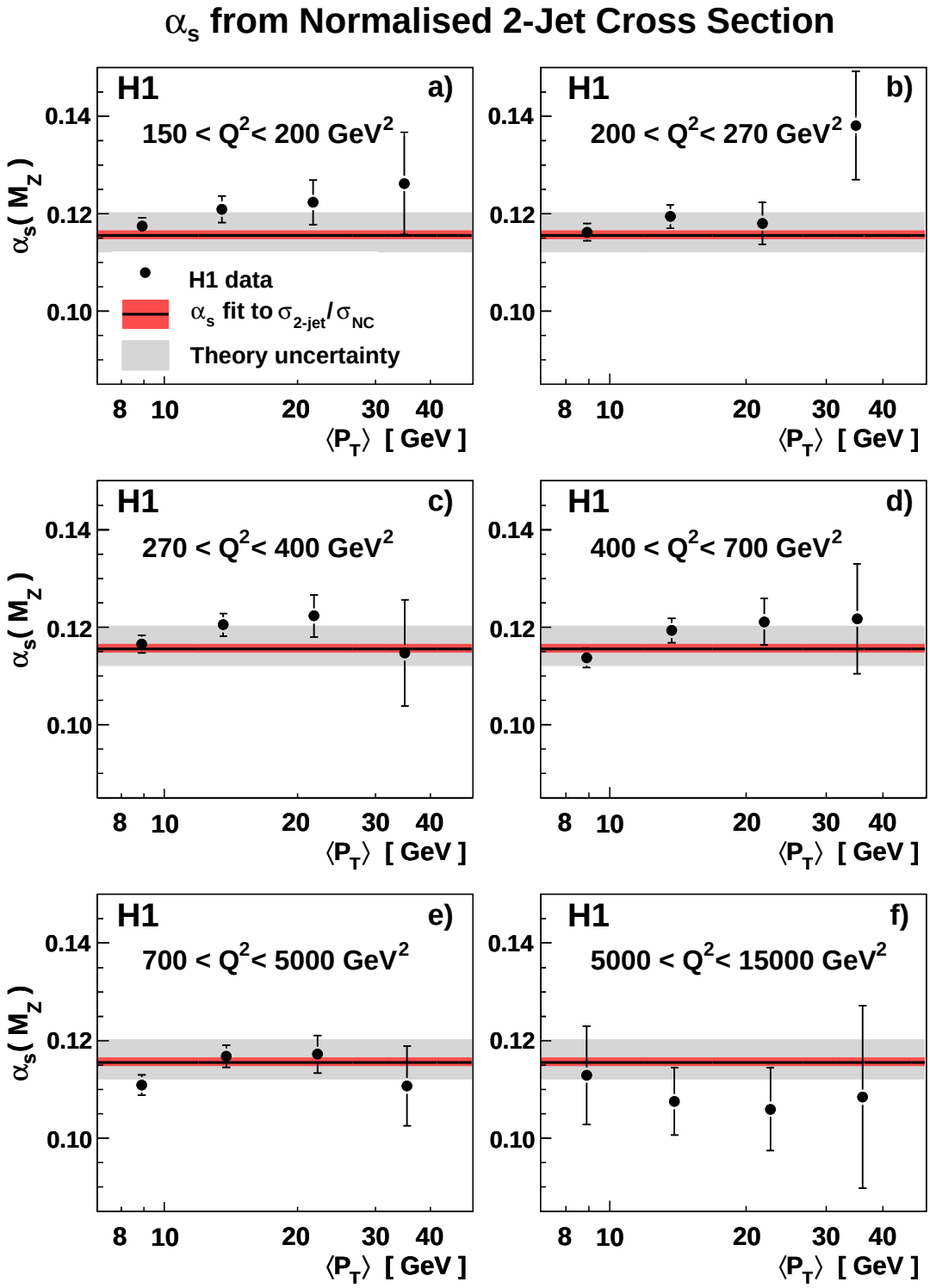

Figure 9: The $\alpha_s(M_Z)$ values determined using the normalised 2-jet cross sections measured in 24 bins in Q^2 and $\langle P_T \rangle$. The solid line shows the two loop solution of the renormalisation group equation, $\alpha_s(M_Z)$, obtained from a simultaneous fit of all 24 measurements of the normalised 2-jet cross sections. Other details are given in the caption to figure 7.

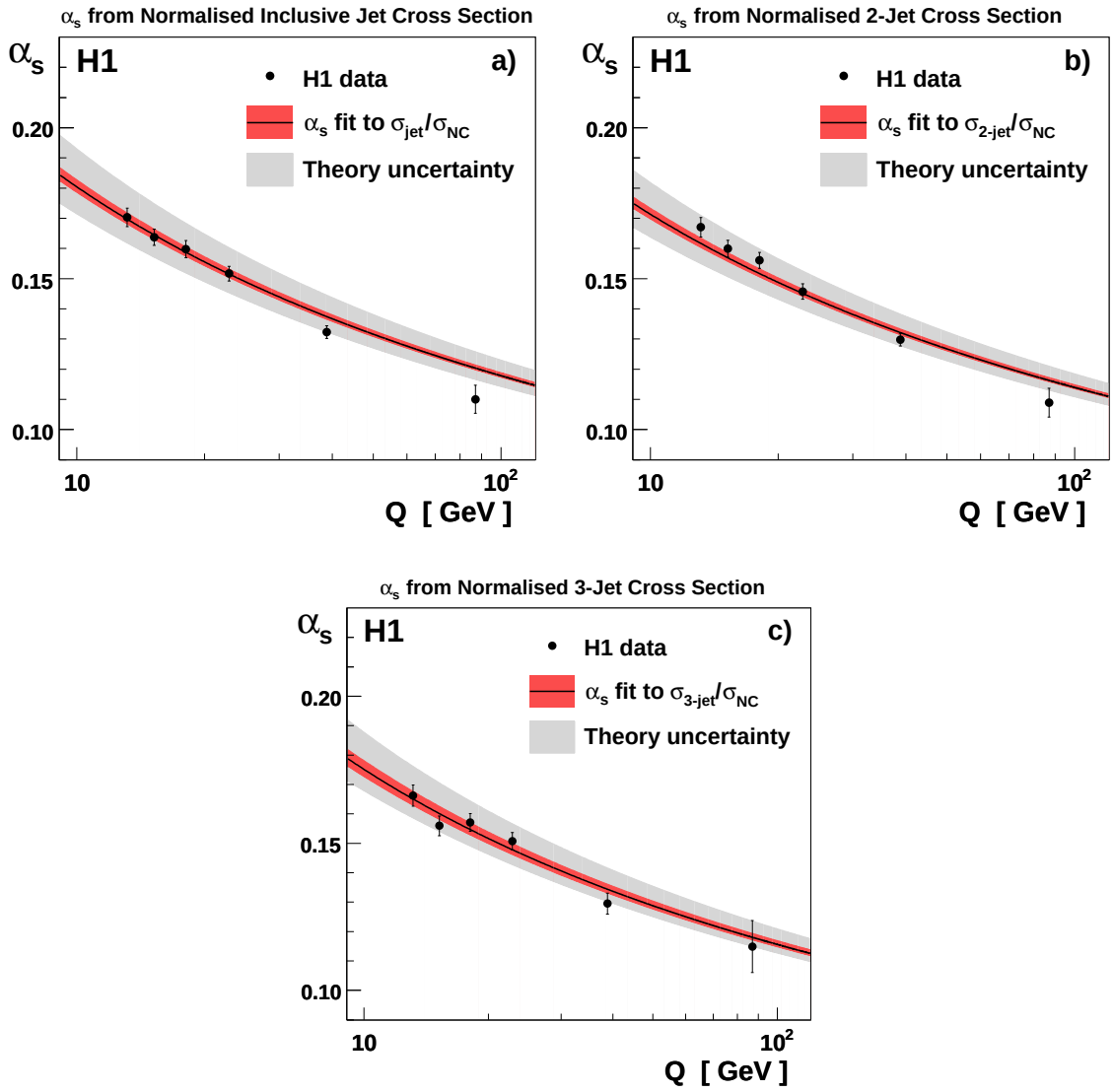

Figure 10: The $\alpha_s(Q)$ values extracted by fitting the P_T dependence of the normalised inclusive jet cross section in different regions of Q^2 (a); $\alpha_s(Q)$ values extracted by fitting the $\langle P_T \rangle$ dependence of the normalised 2-jet cross section in different regions of Q^2 (b); $\alpha_s(Q)$ values extracted from the normalised 3-jet cross section in different regions of Q^2 (c). In each case, the solid lines shows the two loop solution of the renormalisation group equation obtained by evolving the corresponding central value of the $\alpha_s(M_Z)$. Other details are given in the caption to figure 7.

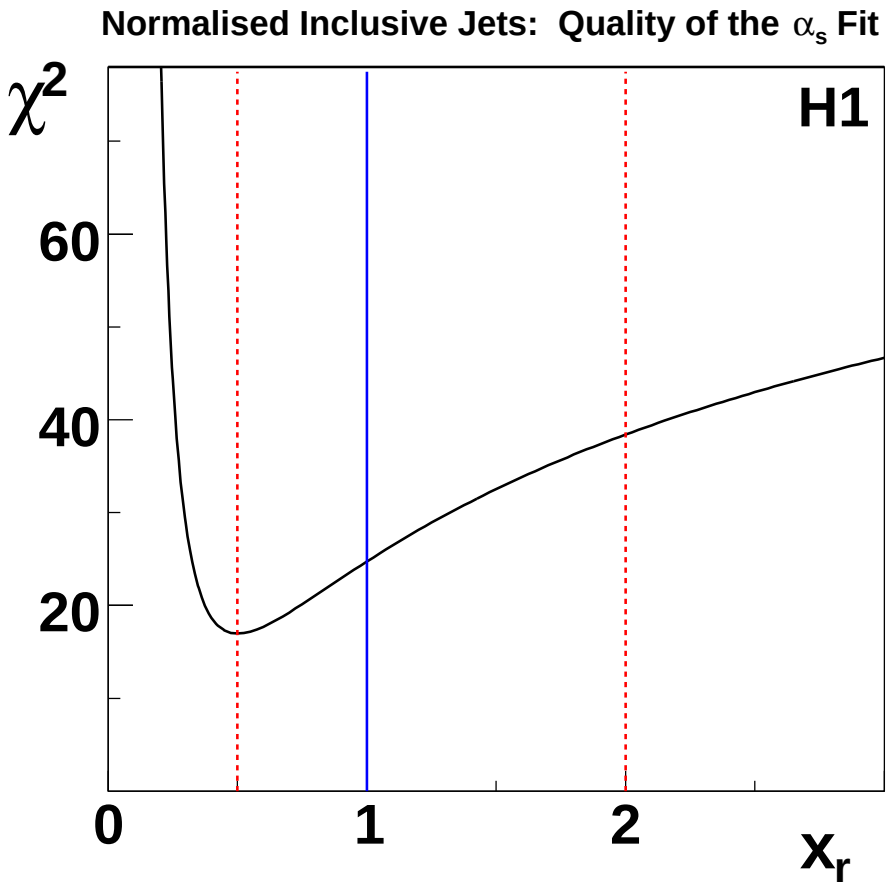

Figure 11: The minimal χ^2 of the fit of the NLO prediction with $\mu_r = x_r \cdot \sqrt{(Q^2 + P_T^2)/2}$ to the normalised inclusive jet cross section as function of x_r for 23 degrees of freedom. Vertical dashed lines represent the range where the renormalisation scale is varied in order to estimate the impact of missing orders beyond NLO, while the full line indicates the nominal choice of the scale with $x_r = 1$.

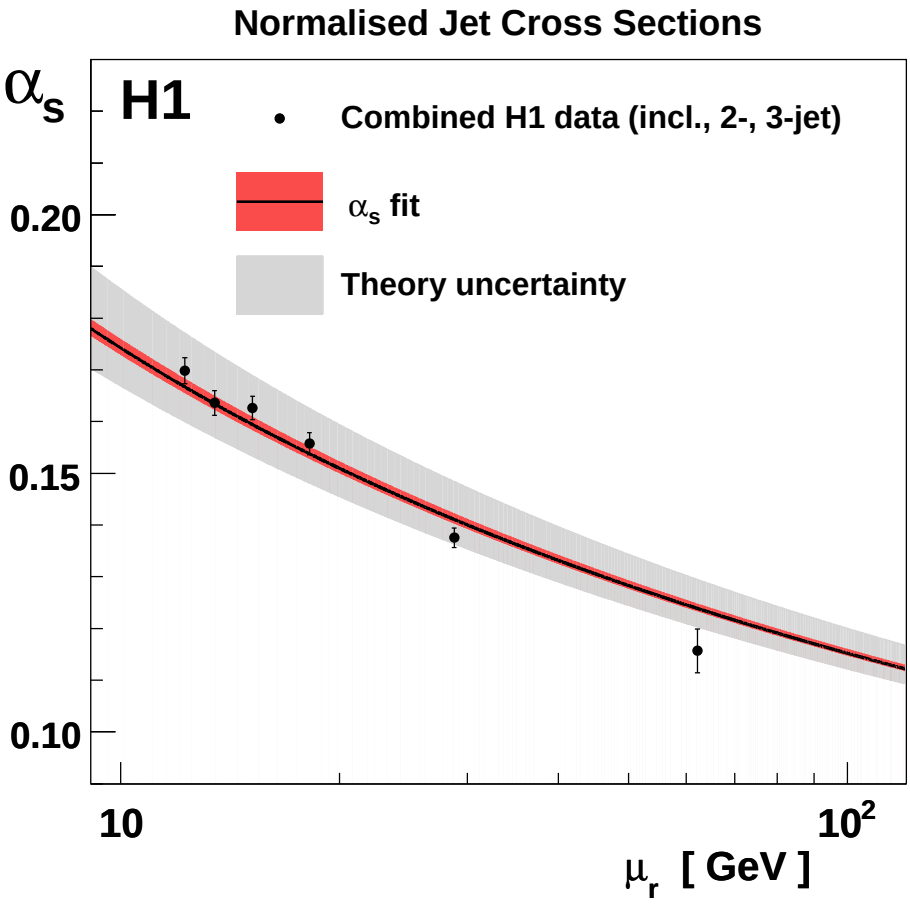

Figure 12: The values of $\alpha_s(\mu_r)$ obtained by a simultaneous fit of all normalised jet cross sections in each Q^2 bin. The solid line shows the two loop solution of the renormalisation group equation obtained by evolving the α_s extracted from a simultaneous fit of 54 measurements of the normalised inclusive jet cross section as a function of Q^2 and P_T, the normalised 2-jet cross section as function of Q^2 and $\langle P_T \rangle$ and the normalised 3-jet cross section as function of Q^2. Other details are given in the caption to figure 7.